Ultrasound Imaging Operation Capture and Image Analysis for Speckle Noise Reduction and Detection of Shadows

by

©Maryam Alruhaymi

A Thesis
submitted to the School of Graduate Studies
in partial fulfillment of the requirements for the degree of

Master of Engineering

Faculty of Engineering and Applied Science

Memorial University of Newfoundland

May 2018

St. John's Newfoundland and Labrador

Abstract

Ultrasound is becoming increasingly important in medicine, both as a diagnostic tool and as a therapeutic modality. At present, experienced sonographers observe trainees as they generate hundreds of images, constantly providing them feedback and eventually deciding if they have the appropriate skills and knowledge to perform ultrasound independently.

This research seeks to advance towards developing an automated system capable of assessing the motion of an ultrasound transducer and differentiate between a novice, an intermediate and an expert sonographer. The research in this thesis synchronizes the ultrasound images with three depth sensors (Microsoft Kinect) placed on the top, left and right side of the patient to ensure the visibility of the ultrasound probe. Videos obtained from the three categories of sonographers are manually labeled and compared using Studiocode Development Environment to complete the items on the medical form checklist.

Next, this thesis investigates and applies well known techniques used to smooth and suppress speckle noise in ultrasound images by using quality metrics to test their performance and show the benefits each one can contribute. Finally, this thesis investigates the problem of shadow detection in ultrasound imaging and proposes to

detect shadows automatically with an ultrasound confidence map using a random walks algorithm. The results show that the proposed algorithm achieves an accuracy of automatic detection of up to 85%, based on both the expert and manual segmentation.

Dedication

I dedicate this thesis to the three pillars of my life: God, my dad, and my mom:

Without you, my life would fall apart. I might not know where life's road will take me, but walking with you through this journey has given me strength.

Dad, you are everything for me; without your love your support and understanding, I would not be able to make it. I never forget that you always told me to "reach for the stars." I think I found my first one.

Mom, you are the only one in the world who gives me joy in my heart and love without end. You have given me so much; thanks for your trust in me, and for teaching me that I should never surrender. I love you more than enough.

Acknowledgements

This thesis could not be realized without reconciliation and a great deal of guidance from “Allah” to complete this work.

My deepest gratitude is to my supervisor, Dr. Mohamed Shehata for the opportunity of working on this interesting topic. He has held me to a high research standard, enforcing strict validations for each research result and thus teaching me how to do research. I am deeply grateful to him for insightful comments and constructive criticisms at different stages of my research.

I must acknowledge as well Dr. Andrew Smith who has truly supported me, directing me to the ultrasound imaging world, helping me improve my background in this area. My sincere thanks goes to him for offering me the whole image database and for teaching me some of the medical aspects needed for this project.

Most importantly, none of this would have been possible without my parents Ghareeb and Salihah and their continuous prayers for me. My immediate family to whom this dissertation is dedicated has been a constant source of love, concern, support and strength all these years.

I would like to express my heartfelt gratitude to my brothers and sisters, Sharef, Mohammed, Ahmad, Nouf, Fatimah, Asma, Sumayyah, Shayma and Shahad for their prayers, collective encouragement and advice. Special thanks from the bottom of my heart to my sister Fatimah who accompanied me during my studies in Canada; we have become good friends and are always willing to try something new to make our life a wonderful world.

I would be remiss if I did not extend my thanks and a warm appreciation to my best friends ever Raghad Alnefaie and Shayiqah Aldarbi for their motivation and insightful guidance.

This research has been funded by the Saudi ministry of higher education. I would like to extend my profuse thanks to the Saudi Arabian Cultural Bureau in Canada for providing full support in carrying out my research work.

Table of Contents

List of Tables

List of Figures

Chapter 1

Introduction and Overview

1.1 Introduction

Ultrasound imaging is being widely used for many clinical applications in a rapid, inexpensive, non-ionizing, and non-invasive manner. Since the ultrasound has become increasingly important in medicine, both as a diagnostic tool and a therapeutic modality, using the ultrasound provides interactive and timely information during surgical procedures. Detailed images of a variety of organs can be obtained when ultrasound waves are directed towards the organ while in contact with the skin. Ultrasound waves can not travel through bone or air in general. However, image quality and interpretation is highly dependent on the operator's skill.

In this research, several depth sensors are used to track the ultrasound transducer during image generation. Kinect's were placed on the top, left and right side of the patient to ensure the visibility of the ultrasound probe (See Fig 1.1). The Kinect is a motion sensing input device by Microsoft, made for the Xbox 360 video game console and Windows PCs. Based on a webcam-style add-on peripheral for the Xbox 360

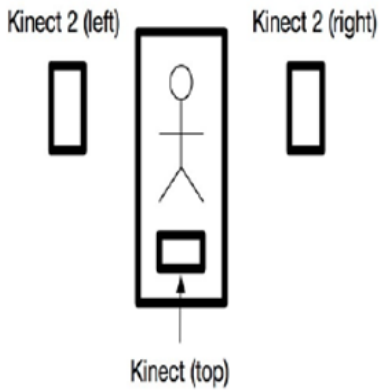

Figure 1.1: An overview of experimental design.

Figure 1.2: Left: Kinect v1, Right: Kinect v2.

console, it gives users control and interacts with the Xbox 360 without the need to touch a game controller, through a natural user interface using gestures and spoken commands (See Fig 1.2) [23].

In addition, one of the major factors limiting visual perception and processing in the ultrasound image is a speckle noise. These noises can cause signal and image degradation, not only in an ultrasound image but also in many medical image modalities [28]. Some of the filtering techniques are used to suppress and smooth speckle noise in ultrasound images by using quality metrics to test their performance and show the benefits each one can contribute.

Furthermore, when the ultrasound hits an object such as bone or air, the energy is completely forming an acoustic shadow deep to the highly reflective surface. Shadow-

ing is normally pronounced in ultrasound images, contributes to diagnosis and can be helpful in grading image quality. Therefore, the detection of these shadow regions is of high importance. In this thesis, automatic shadow detection in ultrasound images is carried out using a confidence map with random walks. Consequently it is compared with manual shadow identification to estimate the accuracy of the algorithm.

1.2 Research Motivation

The quality of collecting data inside operating room impacts every decision made to evaluate the skills of the person doing the scan. Consequently, there is a need for solutions to facilitate data collection and evaluate scanning skills for research studying and analysis. The demand for accurate and reliable data has been more important. Using ultrasound provides interactive and timely information during surgical procedures. In addition, depth sensors (Microsoft Kinect) interpret body movements into a language the computer understands, removing the need for a remote control. This is perfect for the operating room because it means surgeons don't have to leave the sterile field to check scans of the patient. In short, it becomes a hands-free GPS system in surgery. Subsequently, this research seeks to advance towards developing an automated system capable of assessing the motion of an ultrasound transducer and differentiate between a novice, an intermediate and an expert sonographer.

1.3 Thesis Contributions

This thesis can be roughly contributed into three parts:

- **Data Collection and Synchronization:** The first part represents collecting and synchronizing data from three kinects capable of tracking the ultrasound transducer during image generation. The videos obtained from the three categories of sonographers are manually labeled and compared using Studiocode Development Environment with a performance checklist.

- **Speckle Noise Reduction:** The second part investigates noise reduction on ultrasound images. During the image acquisition and transmission process, noise was observed to be one of the more important factors affecting ultrasound images. In this thesis, we discuss six filters namely, Median, Gaussian, Average, Log, Wiener and N-D filter for speckle noise reduction and suppression. We calculate image quality metrics to evaluate which filter can contribute.

- **Shadows Detection** The third part addresses an automatic shadow detection method based on ultrasound confidence map using a random walks algorithm. Shadowing is normally pronounced in ultrasound images, contributes to diagnosis and can be helpful in grading image quality. Consequently, detection these shadows can help with low quality image acquisitions due to large shadowing artifacts. For qualitative evaluation, the comparison between automatic detection and manual segmentation is proposed to demonstrate the accuracy of the algorithm.

1.4 Thesis Organization

The thesis is organized as follows:

- Chapter two provides some background information on basic ultrasound physics and a review of the literature on ultrasound image analysis.
- Chapter three demonstrates the method of study ultrasound imaging operation capture and image analysis for speckle noise reduction and detection of shadows.
- Chapter four explains and discusses the experimental results. We obtained the solution of data collection by synchronized system inside operating room. Applying multiple filters and using confidence maps can be solved the problem of ultrasound imaging quality.
- Chapter five draws the conclusion and recommends future work.

Chapter 2

Background and Literature Review

PartI:

Basic physics of the kinect and ultrasound

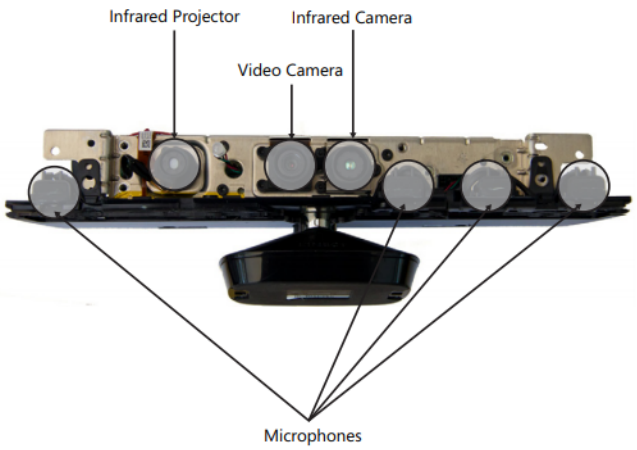

Figure 2.1: The Kinect has two cameras in the middle, a special light source on the left and four microphones are arranged along the bottom of the sensor bar [4].

2.1 Kinect Camera Sensor

The Kinect sensor bar holds two cameras, an infrared light source, and four microphones [23]. It also holds a stack of signal processing hardware with the skill to confirm all the data produced by the cameras infrared source, and microphones. By combining the output from these sensors, a program can track and recognize objects in front of it, determine the direction of sound signals, and isolate them from background noise (See Fig 2.1).

Recently, Microsoft has introduced Kinect v2, which has much enhanced the depth measurement accuracy. Regarding the depth sensing principle, Kinect v1 assumes a structured light method, which projects patterns consisting of many stripes at once, or of arbitrary fingers, and enables the acquisition of a multitude of samples simultaneously [8]. While RGB cameras capture the color information, depth cameras compute the range information between the camera and the object, which presents a more convenient method for three dimensional (3D) model construction and object tracking movement detection.

Figure 2.2: Typical ultrasound machine [1].

2.2 Ultrasound Theory

Ultrasound is an imaging method that uses high-frequency sound waves to produce images of structures within the body. The images can provide valuable information for diagnosing and treating a variety of diseases and conditions [1].

2.3 Diagnostic Medical Sonography

DMS is an imaging technique in which high frequency acoustic energy is transmitted into the body using an ultrasound transducer in contact with the skin, mucous membrane or organ of the patient. The ultrasound waves reflect from tissue interfaces and organs and from regions of differing tissue density. The returning echoes are picked up by the transducer elements and the data generated is used to create an image of the structures and internal organs in different display modes (See Fig 2.2) [1].

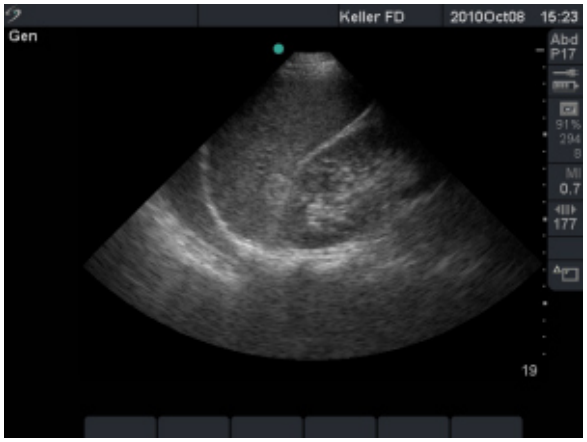

Figure 2.3: B-mode image of the left upper quadrant [49].

2.4 B-Mode Imaging

B-Mode Imaging is termed “brightness mode scanning”; it is known as a 2-D mode or real time gray scale imaging. The 2-D image displayed on the monitor consists of an array of pixels arranged within a linear or sector format. The format depends on the type of transducer used. The intensity of echoes returning to the transducer from the location of a reflective surface is displayed on the image as a level of brightness in a corresponding pixel or group of pixels. The various levels of brightness make up a spectrum of shades of gray that taken together from the image (See Fig 2.3) [49].

PartII:

Literature review

In recent years, many researchers have been interested in the work of ultrasound imaging analysis for different aims and with varying techniques [15][16]. Many applications demonstrated how ultrasound has been developed, not only as a diagnostic imaging modality but as a therapeutic modality, in which energy is deposited in tissue to induce various biological effects. Some techniques that are used in ultrasound imaging are presented later in this thesis.

2.5 Speckle Noise

Medical imaging suffers the interference of locally correlated multiplicative noises from small scatterers which corrupt the ultrasound image. These noises are commonly called "speckles". In many cases, the speckle noise degrades the fine details and edge definition, limits the contrast resolution and limits the detectability of small, low contrast lesions in a body and should be filtered out(See Fig 2.4). The multiplicative speckle is converted into additive noise after logarithm compression; the noise is spatially correlated, and has a Rayleigh amplitude propability density function (PDF): [21].

$$P_A(a) = \frac{a}{\sigma^2} \exp\left(-\frac{a^2}{2\sigma^2}\right), a > 0 \tag{2.1}$$

For fully developed speckle magnitude, the mean to standard deviation-pointwise is signal to noise ratio (SNR)=1.9 (5.58 dB).

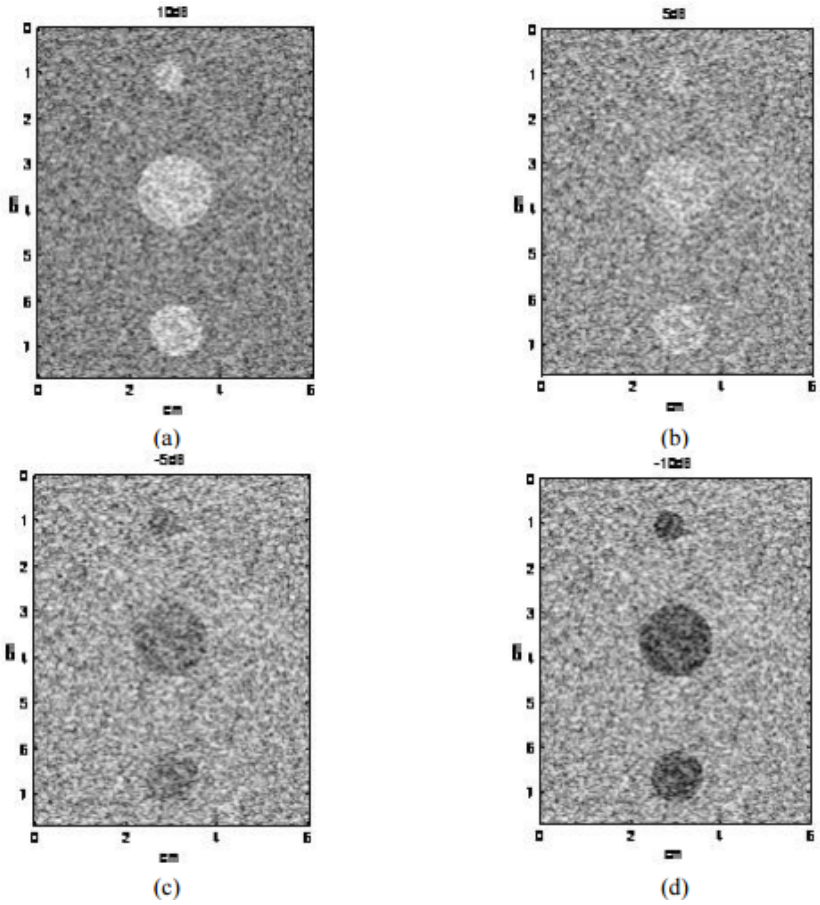

Figure 2.4: Four simulated phantoms with different contrast (a) 10dB, (b) 5dB, (c) -5dB, (d) -10dB [21].

In [21], the authors have implemented four filtering methods:

(1)- Wiener Filter.

(2)- Anisotropic Diffusion Filter.

(3)- Wavelet Filter.

(4)- Adaptive Filter.

The best two images are obtained with Wiener Filter and Anisotropic Diffusion Filter.

2.5.1 Wiener Filter

Since the input filter g=1 in the frequency domain, the Wiener filter is:

$$W = \frac{S_{ss}}{S_{ss} + S_{ww}} \tag{2.2}$$

The power spectrum of the underlying image is modeled as:

$$S_{ss} = \frac{\sigma_s^2}{\left(\sqrt{\mu_x^2 + \mu_y^2}\right)^2} \tag{2.3}$$

where σ_s^2 can be replaced by the mean variance of the noised image σ_x^2. μ_x and μ_y are frequency coordinators; the range is $[-\pi, \pi]$. Figure 2.5 shows that most speckles are removed and that inclusions are clearly seen; even for 5dB contrast cases the background is uniform as simulated.

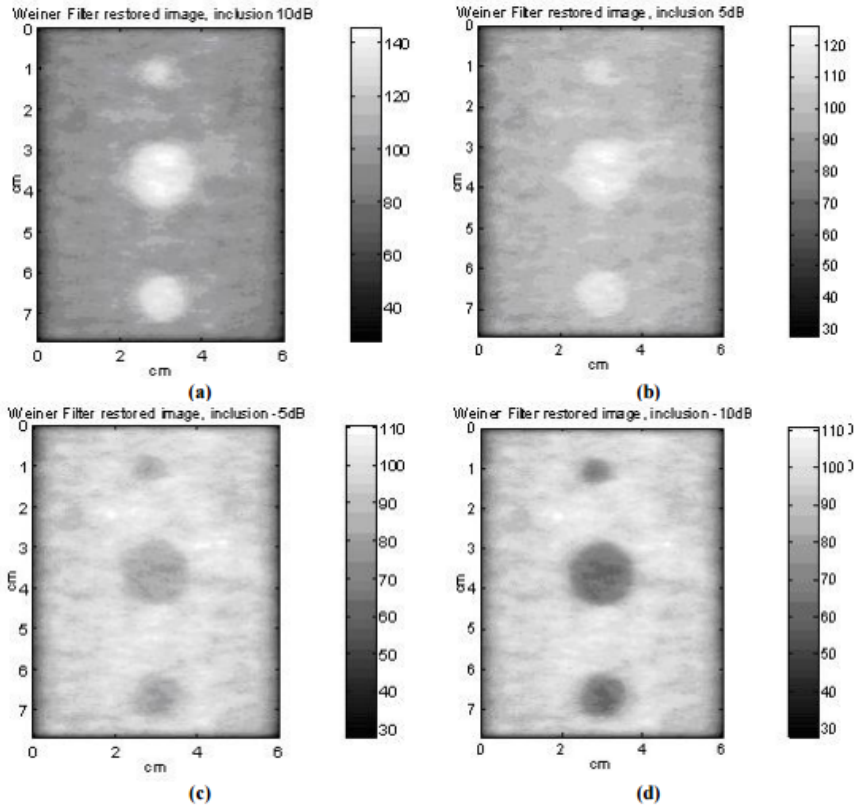

Figure 2.5: Four Wiener filter restored images for simulated phantoms with different contrasts (a)10dB, (b)5dB, (c)-5dB, (d)-10dB [21].

2.5.2 Anisotropic Diffusion Filter

Anisotropic diffusion is an efficient nonlinear technique for simultaneously performing contrast enhancement and noise reduction. It smooths homogeneous image regions and retains image edges.

$$\begin{cases} \frac{\partial I}{\partial t} = div\left[c\left(|\nabla I|\right).\nabla I\right] \\ I\left(t=0\right) = I_0 \end{cases}$$

The main concept of Anisotropic diffusion is the diffusion coefficient. Perona and Malik proposed 2 options:[22]

$$c\left(x\right) = \frac{1}{1+\left(x/k\right)^2}$$

or

$$c\left(x\right) = \exp\left\lfloor -\left(x/k^2\right)\right\rfloor \tag{2.4}$$

The anisotropic diffusion method can be iteratively applied to the output image:

$$I^{(n+1)} = I^{(n)} + \lambda \times [c\left(\left|\nabla_{North} I^{(n)}\right|\right).\nabla_{North} I^{(n)} + c\left(\left|\nabla_{East} I^{(n)}\right|\right).\nabla_{East} I^{(n)}$$

$$+c\left(\left|\nabla_{West} I^{(n)}\right|\right).\nabla_{West} I^{(n)} + c\left(\left|\nabla_{South} I^{(n)}\right|\right).\nabla_{South} I^{(n)}] \tag{2.5}$$

This filter method can restore a noised image well and gives better contrast while removing speckles effectively (See Fig 2.6). In point of fact, because the parameters in an anisotropic diffusion method are adjustable, parameters can be controlled and the best image chosen. Figure 2.7 shows the comparison of image profile before and after filtering, which obtained smoother images.

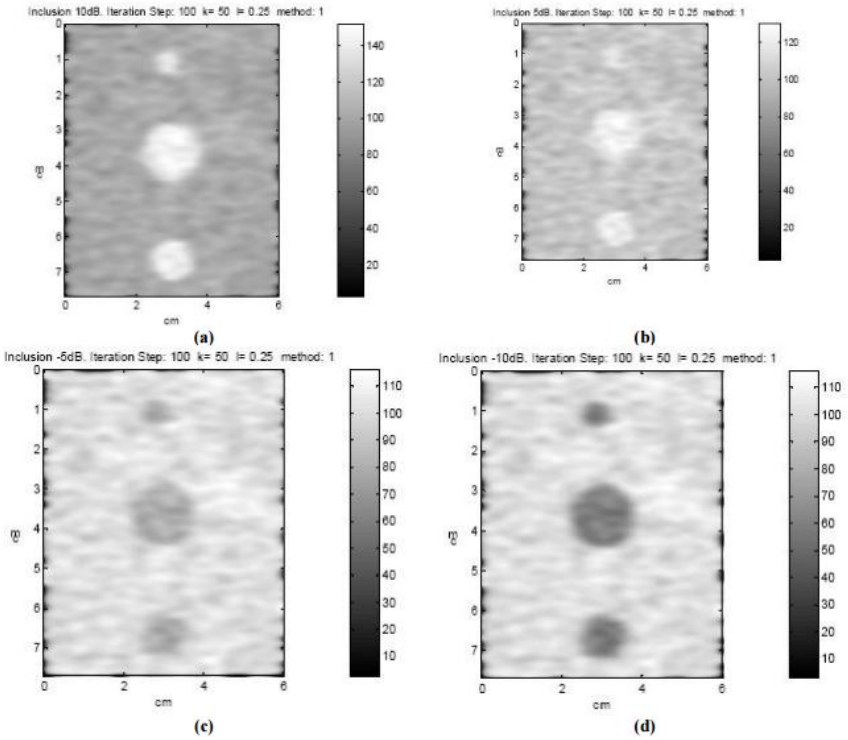

Figure 2.6: Four Anisotropic diffusion filter restored images for simulated phantoms with different contrasts (a) 10dB, (b) 5dB, (c) -5dB, (d) -10dB [21].

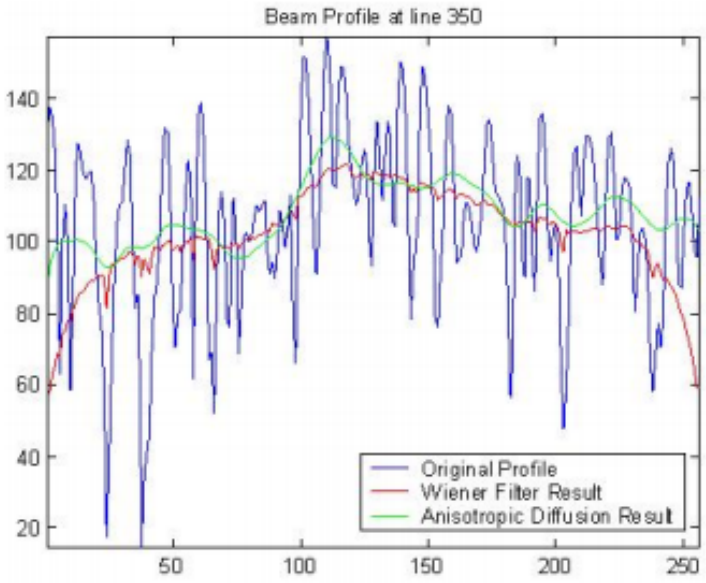

Figure 2.7: The profile before and after filtering [21].

2.6 Shadow Detection

A strong reflector of sound casts an acoustic shadow; there is little energy left to visualize the tissue behind the objects, such as bones and gallstones. The detection of these shadows is useful for diagnosis. There limited literature on automatic methods to detect shadows in medical imaging. Methods can be defined in two ways: Intensity based methods [24][25] and Geometric methods [26] [27]. Intensity based methods rely on a direct analysis of the intensities to detect dark regions. Geometric methods take into account the probe's geometry and analyze intensity profiles along the lines that compose the B-scan. [13] introduced an automatic 2D ultrasound shadow detection method that employs scan line energy and local image entropy information.

2.6.1 Extraction of scan lines

It is necessary to separate the image and the background in ultrasound imaging. [13] has given a sequence of 2D ultrasound images. This amounts to computing a 2D mask given the 2D + t sequence. To do so, maps of longitudinal mean and variance are computed, and multiplied pixelwise to compute a feature map. For a given point, the longitudinal mean is defined as the mean at a 2D pixel location over time. Background pixels are dark and have low (or zero) variance. Points in the image foreground have the highest values of the feature map (compared to the background). Then, points with the highest values of the feature map are retained. Some false detections exist, mainly due to textual data and complementary image information presented on the ultrasound machine display. To extract scan lines of ultrasound images: first, find the left and right boundaries of the trapezoid by thresholding and morphological image opening. Then, fit two straight lines to the left and right borders by minimizing of

mean square error. The probe coordination is derived from the intersection of these two lines. Then, arbitrary scan lines can be drawn at different ultrasound propagation directions, thereby simulating transducer beams.

2.6.2 Line rupture detection

It is required to sample line profiles according to the scan lines drawn and for each line, K samples are computed. For each ultrasound image, an arbitrary number of scan lines can be considered, as more scan lines provide more shadow details. The shadow is defined as a signal rupture along the line, followed by a low signal. Therefore, signal ruptures are detected first. Then, a local symmetric entropy criterion is computed. For each point P of the line signal S , a sliding window of size $n = 5$ is used to compute the rupture criterion R [13] :

$$R = \sum_{i=1}^{i=n} \left(S\left(p-i\right) \log \frac{S\left(p-i\right)}{S\left(p+i\right)} + S\left(p+i\right) \log \frac{S\left(p+i\right)}{S\left(p-i\right)} \right) \tag{2.6}$$

The first term is the relative entropy of the "past"(the signal before the rupture) knowing the "future"(the signal after the rupture) which can also be viewed as the divergence of the past distribution given a reference signal (the future). In order to symmetrize the criterion, the second term is added and expresses the relative entropy of the future knowing the past. The loci where R is maximal indicate a signal rupture. The rupture criterion R is quite general since it relies on the statistical dependency between the future and the past samples in a sliding window. Rupture positions are determined as zero-crossings of the gradient of R. Figure 2.8 illustrates the rupture detection on a synthetic example.

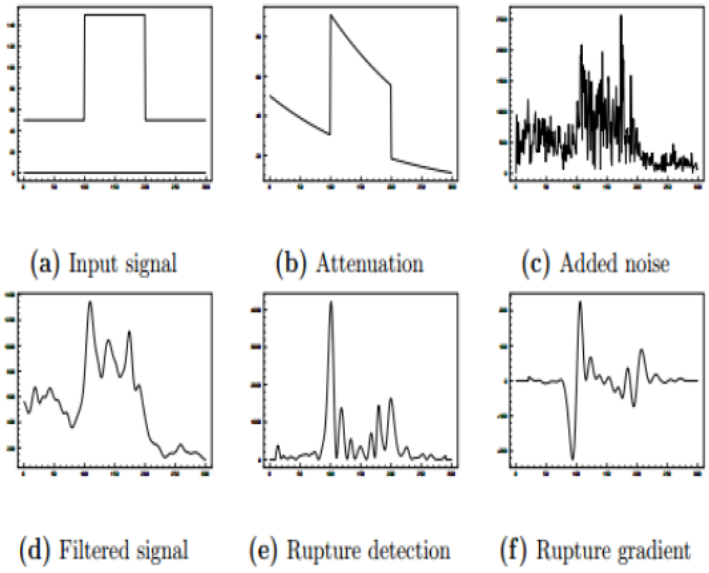

Figure 2.8: Illustration of the line processing on a synthetic signal [13].

2.6.3 Shadow detection

It is generally assumed that acoustic shadows are areas where the ultrasound signal is relatively low. In [13], authors assumed that acoustic shadows are areas where the noise is low. Since noise is modulated by signal intensity in ultrasound images, this is not a strong assumption. When a rupture is detected and tested as a candidate for a shadow, denote $E(uf)$(respectively $V(uf)$) and the mean (respectively the variance) of the signal after the rupture. Figure 2.9 shows the recorded ultrasound that is the input for the shadow detection algorithm and represents the shadow detection result employing the method without and with regularization respectively.

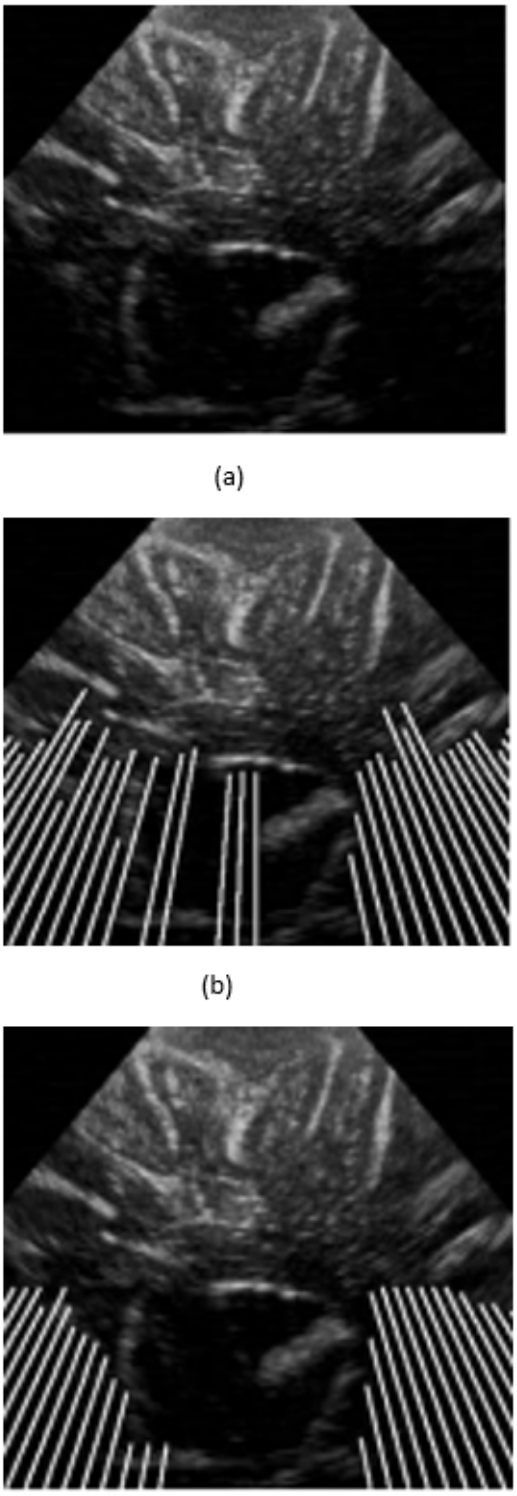

Figure 2.9: (a) Initial B-scan, (b) Raw estimation, (c) Regularized [13].

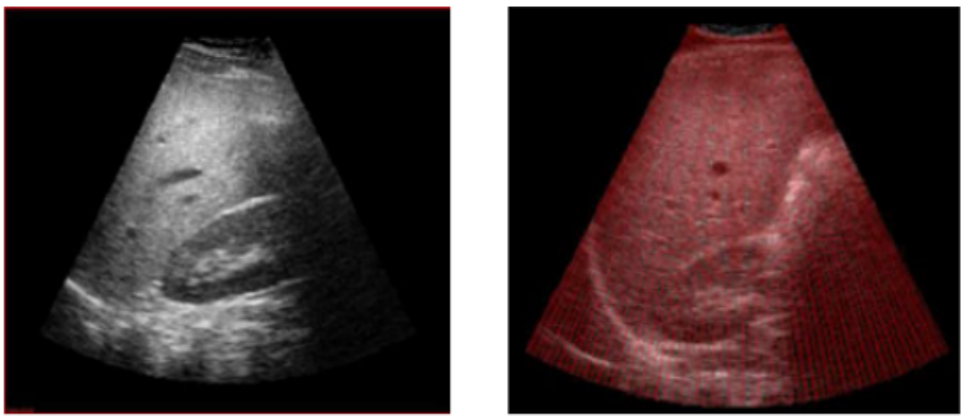

Figure 2.10: (a) An ultrasound acquisition, (b) The XY image direction of a 3D ultrasound [54].

In [54], the authors have proposed a shadow detection method using the previous method [13] but on 3D ultrasound imaging to enhance the accuracy results of shadowing. Figure 2.10 shows a scan line simulation. However, applying this method to 3d US imaging has some weakness, because some scan line signals do not contain any further tissue information that confirm that the shadow detection fails. An example of this behavior can be seen in figure 2.11.

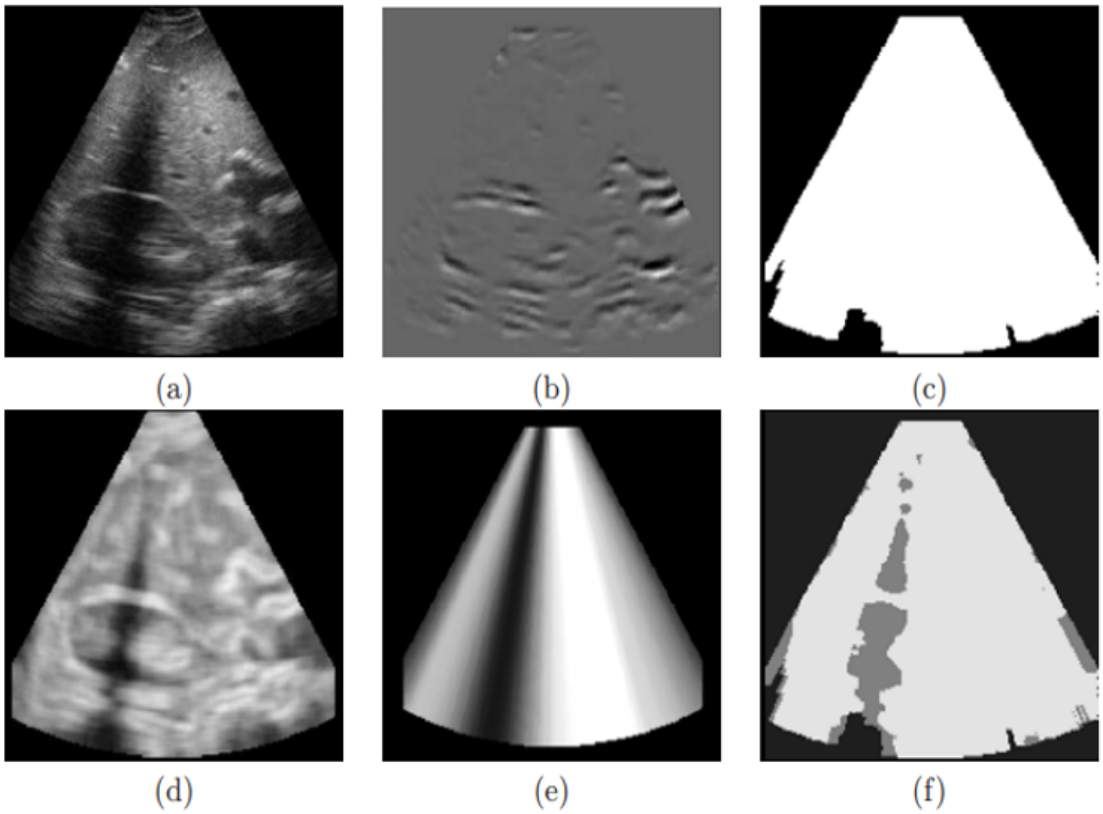

Figure 2.11: (a) Rib shadow occurring in a renal scan, (b) Smoothed rupture criterion calculated for 150 simulated scan lines, (c) Detected shadow mask applying the adopted shadow detection approach [13], (d) Local entropy feature image, (e) Maximum scan line energy image, derived from the accumulated scan line intensities, (f) Improved shadow detection mask of the proposed method with gray values being newly detected shadow regions [54].

Some of the shadow characteristics have been added to the approach to enhance the results of shadows on a 3d ultrasound acquisition as follows:

(•)- Introduced a new value (127), which marks a possible shadow candidate.

(•)- Used a neighborhood radius of 3 pixels and a Rayleigh probability distribution function.

(•)- Calculated the maximum possible entropy value to obtain percentage entropy thresholds.

(•)- calculated the accumulated intensity profile for each scan line.

Figure 2.12 shows the result of the shadow detection method applied on 3d ultrasound images. The enhancement algorithm presented all gray (127) mask values that presented a new shadow information (See fig 2.12 (d)-(f). The previous method only detected tissue values (255) (See Fig 4.12 (c) and (f))[13]. In [54], the authors achieved a significantly improved shadow detection that outperforms the adopted literature approach.

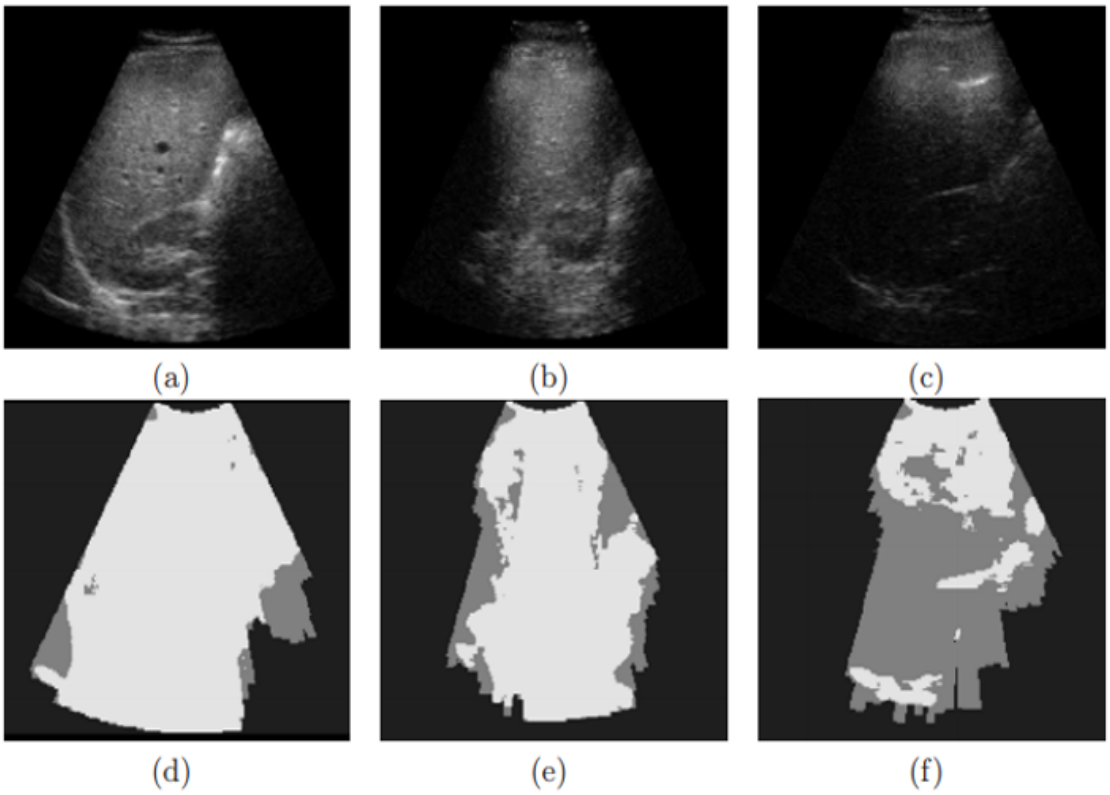

Figure 2.12: Detection matrix with the input ultrasound (a)–(c) and the detection results (d)–(f) of the proposed method for minor, medium and severe shadow artifacts [54].

.

2.7 Automatic Shadow Detection in IVUI

In another work, an automated algorithm for shadow region detection in Intra Vascular Ultrasound images was described using an adaptive threshold method [17]. The algorithm investigated three aspects in IVUS: (1) Catheter zone, (2) Calcification region, (3) The border of shadow. The catheter zone and calcification region consist of high gray levels in IVUS images. However, some bright regions such as parts of catheters may be wrongly detected. Use of a Circle Hough Transform can avoid this problem, to detect the catheters zone. The calcification region was segmented by the Otsu method. Finally, an active contour is used to detect the border of shadow [40].

2.7.1 A. Preprocessing

The catheter artifact must be removed as a first step. The Circle Hough Transform (CHT)can be used. The area of the circle must be identified by applying CHT to speed up the calculations. In the next step, the Otus method is utilized to automatically find the optimal level for the threshold and to detect the catheter zone.

(1). Otsu Threshold Method

An automatic global threshold method has been developed by the author in [41]. His technique calculates the optimum threshold separation based on the global property of the histogram. Only the zero and the first order cumulative moments of the gray-level histogram are used. The total number of pixels in the image is denoted by N and the number of pixels at with gray level is shown by ni :

$$N = V_1 + V_2 + ... + V_n \tag{2.7}$$

The gray-level histogram is normalized and regarded as a probability distribution:

$$P_i = \frac{n_i}{N}, P_i \geq 0, \sum_{i=1}^{L} P_i = 1 \tag{2.8}$$

The pixels are divided into classes $C0$ and $C1$ (background and object, or vice versa) by a threshold at the gray level k; $C0$ denotes pixels with gray levels $[1, ..., K]$, and $C1$ denotes pixels with levels $[K+1, ..., L]$. Then the probabilities of class and the class mean gray levels, respectively, are given by:

$$w_0 = Pr\left(C_0\right) = \sum_{i=1}^{k} P_i = w\left(K\right) \tag{2.9}$$

$$w_1 = Pr\left(C_1\right) = \sum_{i=k}^{L} P_i = 1 - w\left(K\right) \tag{2.10}$$

and

$$\mu_0 = \sum_{i=1}^{K} iPr\left(i|C_0\right) = \sum_{i=1}^{K} \frac{iP_i}{w_0} = \frac{\mu\left(K\right)}{w\left(K\right)} \tag{2.11}$$

$$\mu_1 = \sum_{K+1}^{L} iPr\left(i|C_1\right) = \sum_{i+K}^{L} \frac{iP_i}{w_1} = \frac{\mu_T - \mu\left(K\right)}{1 - w\left(K\right)} \tag{2.12}$$

where $A\left(K\right)$ and $\mu\left(K\right)$ are the zero-th and first order cumulative moments of the histogram up to the k-th level:

$$w\left(K\right) = \sum_{i=1}^{K} P_i \tag{2.13}$$

and

$$\mu\left(K\right) = \sum_{i=1}^{K} iP_i \tag{2.14}$$

and μ_T is the total mean level of the original image.

$$\mu_T = \sum_{i=1}^{L} = iP_i \tag{2.15}$$

The optimal threshold is determined by the value that maximizes the between-class variance:[41]

$$\sigma_B^2(K) = \frac{[\mu_T w(K) - \mu(K)]^2}{w(K)[1 - w(K)]} \tag{2.16}$$

Therefore, the optimal threshold K^* is defined by:

$$\sigma_B^2(K^*) = max_{0 \le K < L} \sigma_B^2(K^*) \tag{2.17}$$

The catheter zone is detected by thresholding with K^* value.

(2). The Circle Hough Transform

One of the most common algorithms to detect circle shape is CHT [40]. The transform is computed by using the features of edges in the image, and the peaks in the transformed image correspond to the centers of circular features of the image. A circle with radius R and center (a, b) can be described by the parametric equations.

$$(X_P - a)^2 + (Y_P - b)^2 = R^2 \tag{2.18}$$

where X_P and Y_P are the coordinates of the pixel of edges, "a" and "b" are the coordinates of the center of the circle which is also the center of the image in this data and R is the radius of the circle.

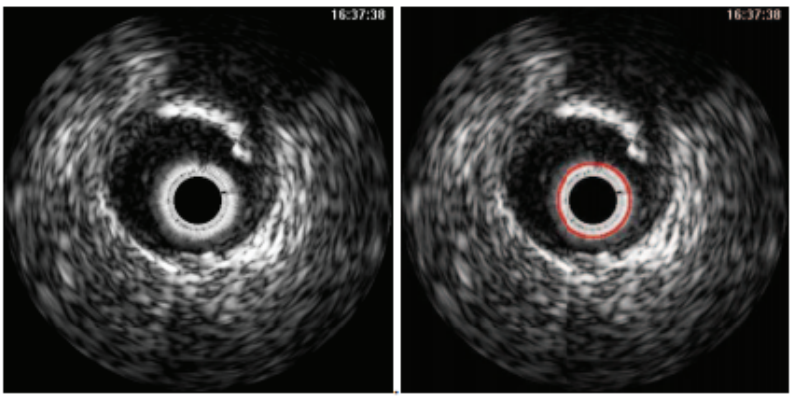

Figure 2.13: (a) A typical intravascular ultrasound image, (b) An example of catheter zone detection by CHT [17].

(3). Catheter Artifact Removal

A constant radius and the full circle are obtained using the Circle Hough Transform, but the size of the catheter zone varies in each image. Therefore, a partial circle with a large radius in the parameter space produces a larger number than a complete circle with a small radius. To solve this problem, the number of pixels in each detected circular object is divided by the number of pixels in the full circle with the same radius. This provide a rate of circularity of the object:

$$Rate of circularity = \frac{Npd}{Npc} \tag{2.19}$$

where Npd is the number of pixels of the detected circular object and Npc is the number of pixels of a complete circle with the same radius. The maximum number in the "rate of circularity" parameter gives the maximum radius of catheter as in figure 2.13.

2.7.2 B. Calcification region detection

Applying threshold methods can be detected the calcification regions which have a high gray level in IVUS images. However, the level of the threshold is different for each image, so an adaptive threshold has been used. [33] has developed a multi scale segmentation method for calcification detection.

2.7.3 C. Detection of acoustic shadow

The acoustic shadow presents a low value of median while the shadow region appears as a dark region. The following algorithm was applied:

(1). Determining rightmost and leftmost points of segmented objects.

(2). Determining the lowest points of segmented objects.

(3). Determining the center of segmented objects.

(4). Calculating the median gray level value of a square from the rightmost to leftmost point and from the lowest points of segmented objects to the bottom of the image (See Fig 2.14).

(5). Calculating maximum gray level value in 7×7 window surrounded centroids.

(6). If $\frac{med}{max_{cen}} \leq Th$, then classify the segmented object as a calcification accompanied by an acoustic shadow.

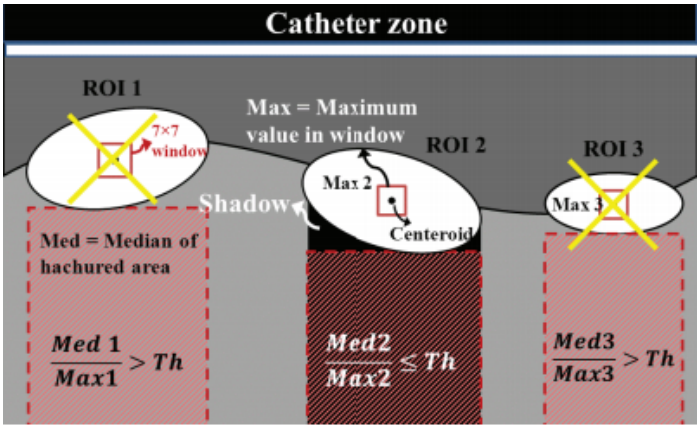

Figure 2.14: Example of detection of calcification due to acoustic shadow [17].

2.7.4 D. Shadow border detection

It is very common to apply active contour models to solve computer vision problems, including image segmentation, edge detection and visual tracking [50] [52]. In contrast, [53] has applied an active contour without an edge model to identify the shadow region. The idea is to choose an initial curve(a square or a circle)and then deform this edge to get the object's edge. In order to detect the border of the acoustic shadow, the active contour has been initialized by a 5×5 window in the middle of the hachured area as shown in figure 2.15.

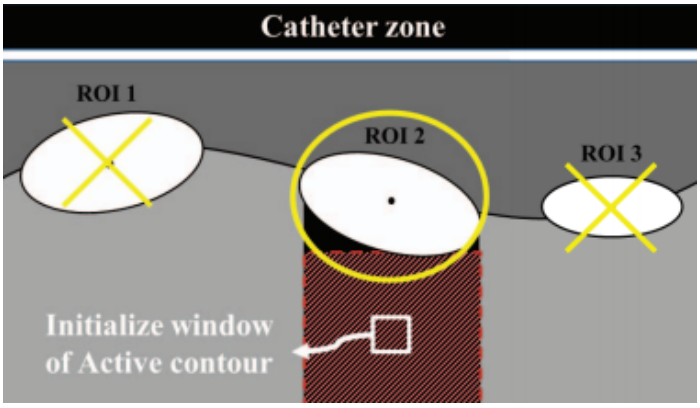

Figure 2.15: Example of initialization window of active contour in shadow border detection [17].

Figure 2.16 shows the shadow regions as automatically segmented and compared with experts' results. The results of the test are summarized in table 2.1.

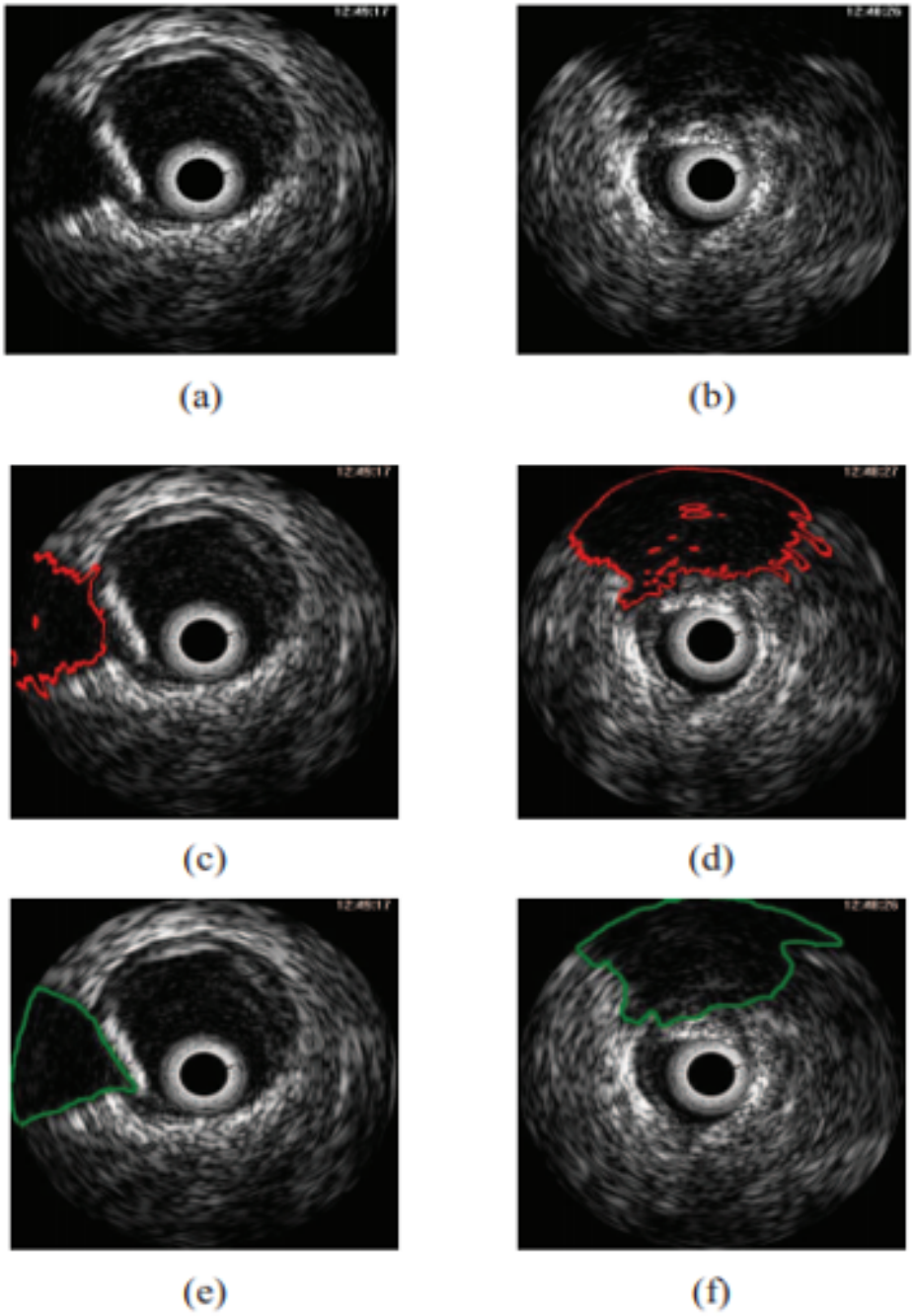

Figure 2.16: Example of detecting border of shadow in intravascular image. (a,b) are the original images, (c,d) are the corresponding automatically segmented images, (e,f) are the corresponding manually segmented images [17].

Table 2.1: Table of results

	Number of data	Regions correctly classified	Regions incorrectly classified
Shadow region	15	14	1
Normal tissue	15	13	2

Chapter 3

Experimental Setup and Proposed Methods

3.1 Data Collection and Synchronization

In this step of the research thesis, ultrasound images and depth images from three sides of the patient are collected and synchronized to ensure the visibility of the US probe. Ultrasound and color images are used for both medical evaluation and movement analysis, while depth images are dedicated to movement analysis. The overview of this step is illustrated in figure 3.1. Two Kinects 2 are placed on both sides of the patient and another Kinect is mounted above the patient. Because of the USB bandwidth limitations, only one Kinect was connected to each laptop. Thus, a distributed network is built to enable data collection from multiple high-bandwidth devices.

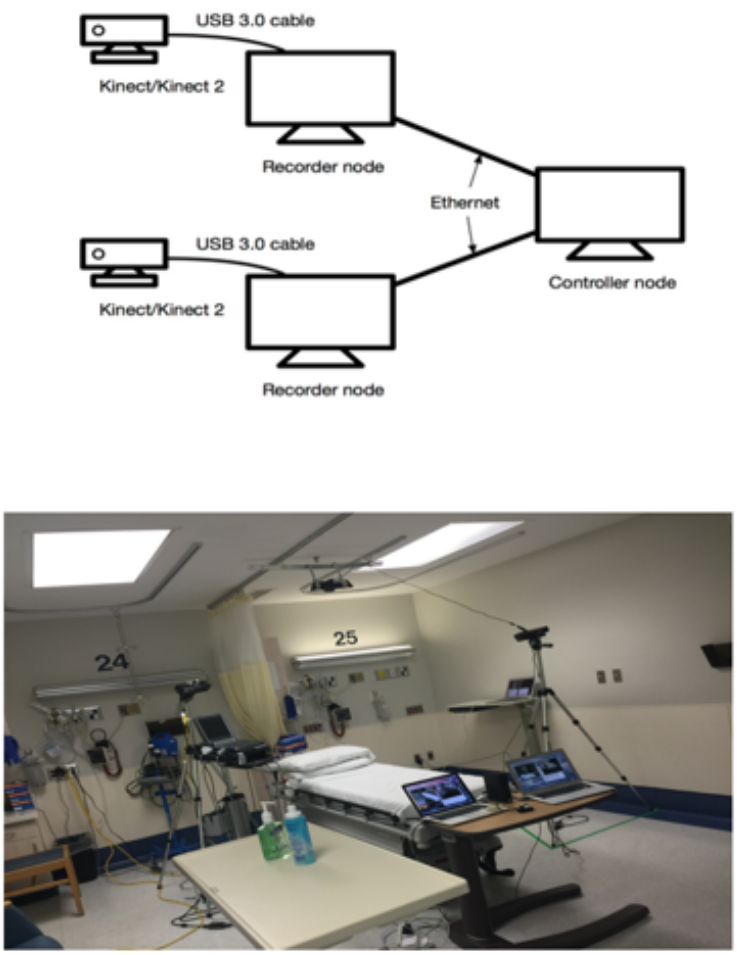

Figure 3.1: System design

The computers used are classified into two classes: collecting nodes and control nodes; collecting nodes wait for commands from a control node at the same time to ensure the data collections are started and stopped at the same time. Collected data are written to collecting nodes' local hard disk drivers. These files are named with the UNIX timestamp. To make sure the timestamps consist of all collecting nodes, NTP (Network Time Protocol) is used to synchronize the RTC (Real-time clock) of all nodes. The format of saved data is motion JPEG. Each frame is saved as an independent JPEG file on disk and named with the current timestamp. Two collecting nodes control two Kinect2 because each Kinect2 consumes approximately 50% of the USB 3.0 bandwidth. The remaining devices (US and Kinect) are controlled by another collecting node. The control node program also runs on that computer. When an experiment begins, the control node sends a 'start' command to all collecting nodes. Collecting nodes show 'recording' on screen indicating the recording has begun. A folder is created on each collecting node and all frames are saved into that folder. The control node sends a 'stop' command to each collecting node when the experiment is finished. Another program converts these frames into a video file with interpolation to ensure the consistency of the frame-per-second parameter. The videos will be used for further analysis.

3.2 Studiocode Development Environment

Studiocode is a much improved way of reviewing and analyzing role play of a simulation's recorded video. It is video coding software that allows the use of either live stream video or pre-recorded video. In addition, Studiocode enables the playing of multiple different videos side by side for comparison during coding. This is particularly useful if different vantage points or angles of the same event are being coded.

The key benefits of studiocode video analysis software are as follows:

- Increases the accuracy of observations,
- Improves the quality of feedback,
- Reinforces the training,
- Provides a permanent record and
- Demonstrates improvements.

In this work, it is outlined more fully in a later chapter how studiocode is used to analyze video data of sonographers inside an operating room to complete the items of the training checklist.

3.3 Speckle Noise Reduction

In the last few decades, several techniques for speckle noise reduction and suppression have been developed. In 2006, research produced speckle reduction with using two approaches:
(1) the compounding approach, (2) the post processing approach [29]. The compounding approach includes methods in which the data acquisition procedure has been modified to produce several images of the same region and combine them to form a single image [30]. The post-processing approach includes many different filtering techniques that are implemented on the B-mode images after they have been generated. They are divided mainly into two classes:[31]

(i) Techniques that are applied directly in the original image

(ii) Techniques that are applied in the frequency domain.

Latterly, the post formation filtering methods applied directly to the original image have been the focus of much research. Techniques in this approach include many fixed and adaptive filters,such as adaptive filter reduction (AFR),an adaptive weighted median filter (AWMF) and nonlinear diffusion.[32] [34] [35]

One of the main problems when employing an image processing technique is assessing its performance. The quality of a reconstructed image could be measured by the traditional distortion measures such as mean-square error (MSE), peak signal-to-noise ratio (PSNR), and correlation coefficients between the original and reconstructed images [36]. [29] evaluate the effectiveness of speckle reduction in the ultrasound images for each simulated image, by statistically estimating three image quality parameters, contrast to noise ratio (CNR), lesion signal to noise ratio (LSNR) and signal to noise

ratio (SNR), as defined in [37]. The parameter SNR is used to evaluate the improvements in smoothing, as observed in homogeneous regions of an image (speckle region).

Well known techniques of speckle noise in the smoothing or suppression are applied directly in the noise image. A comparison of the methods studied is based on an experiment using quality metrics to test their performance and show the benefits each one can contribute.

In the following subsection, the different types of noise in ultrasound images and the techniques used in this thesis to remove them are described.

3.3.1 Types of noise

There are different types of noise present in the image.

- **Gaussian noise:** shows little variation in the image for reasons such as different sensor gain, quantization errors in digitization, etc. At first sight, a noisy image appears to be the same as the original one but is very different.

- **Multiplicative or Speckle noise:** the result of the multiplication of two signals. In all cases, noise always implies a sudden change in an image's intensity level; thus, noise is considered an image's high frequency component.

- **Poisson noise:** is a basic form of uncertainty associated with the measurement of light, inherent to the quantized nature of light and the independence of Poisson detections. Its expected magnitude is signal-dependent and constitutes the dominant source of image noise, except in low-light conditions.

- **Salt & Pepper noise:** is also known as Impulse noise and can appear when the sensor that picks up the image is saturated and the value of the pixel shows a

high value or when the signal is lost and the pixel shows a low value. In this case, the image has too high or too low pixel values.

3.3.2 Types of filters

A filtering method should be used to remove the unwanted noise. Some types of filters are studied in this thesis.

1. **Median filter** is a nonlinear digital filtering technique, often used to remove noise. Median filtering is very widely used in digital image processing because it preserves edges while removing noise.[37] used the median intensity in a suitably sized and shaped region W_{ij} surrounding the pixel (i, j) of interest as the output pixel value, therefore, eliminating any impulsive artifacts with an area (in pixels) of less than half the region size $\|W_{ij}\|$.

2. **Gaussian filter** is implemented to remove the Speckle Noise present in ultrasound images. In this technique, the average value of the surrounding pixels or neighboring pixels replaces the noisy pixel present in the image, which is based on Gaussian distribution.

3. **Average filter** is a linear filter and a very useful filter for removing certain types of noise. It can remove grain noise from a photograph. Because each pixel is set to the average of the pixels in its neighborhood, local variations caused by grain are reduced [55].

4. **Log filter** is a laplacian filter with a Gaussian filter used to find areas of rapid change. It is commonly used to smooth the image. However, this filter does not acceptably affect noise.

5. **Wiener filter** is a low pass filter that filters images which have been degraded

by constant power additive noise. It helps in inverting the blur and executes the deconvolution with a high pass filter and removes the noise with a compression operation [43].

6. **N-D filter** The imfilter function is used to perform filtering of multidimensional images. It computes each element of the output using a double-precision floating point. It shortens the output element that exceeds certain types of ranges and rounds the fractional value if the original image is an integer or logical array.

3.3.3 Performance analysis

In this subsection, the performance analysis techniques for each filter have been studied using image quality metrics. The metrics used to experiment with images are the well-known mean-square error (MSE), signal-to-noise ratio (SNR) and peak signal-to-noise ratio (PSNR)(See Fig 3.2). The MSE, SNR and PSNR metrics are defined in the following expressions:

$$MSE = \frac{1}{M.N} \sum_{m=0}^{M-1} \sum_{n=0}^{N-1} \left[I(m,n) - \hat{I}(m,n) \right]^2 \tag{3.1}$$

$$SNR = 10. \log_{10} \frac{\frac{1}{M.N} \sum_{m=0}^{M-1} \sum_{n=0}^{N-1} I^2(m,n)}{MSE} \tag{3.2}$$

$$PSNR = 10. \log_{10} \frac{255^2}{MSE} \tag{3.3}$$

In these expressions, I is the original image and $\hat{I}$ is the estimation of the original image obtained from a noisy image. The images measurements are $M.N$.

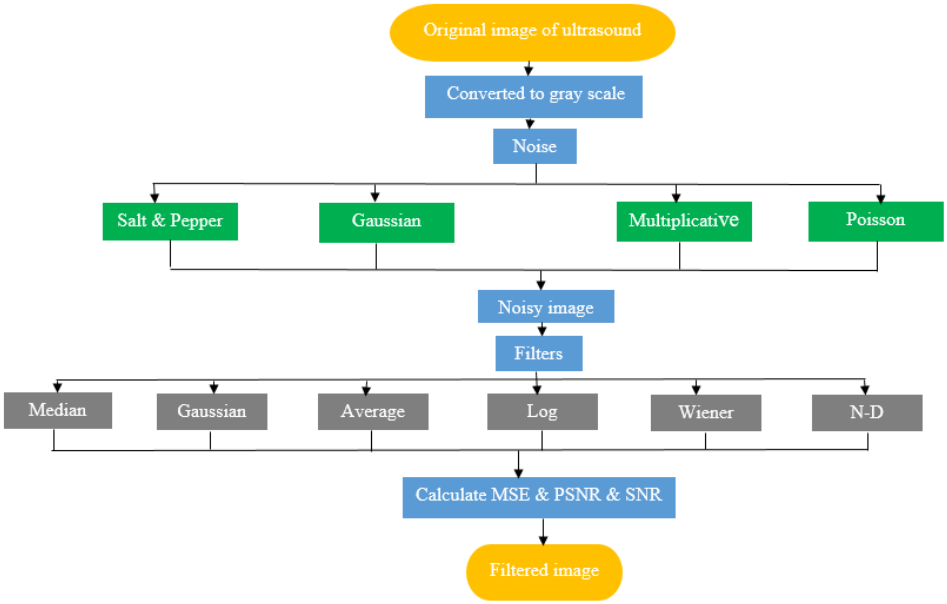

Figure 3.2: Perform work sequence

.

3.4 Ultrasound Shadowing

An utomatic shadow detection in ultrasound images is carried out using a confidence map with random walks. Consequently it is compared with manual shadow identification to estimate the accuracy of the algorithm. The work presented in this section is beyond on the paper by [47] with the following contributions on new novelties:

3.4.1 Temporal compression

Temporal compression takes advantage of areas of the image that remain unchanged from frame to frame, throwing out data for repeated pixels.

- The goal of this approach is to separate the shadows areas and the unreliable information on images.
- While images obtained from confidence map has different appearances of white, gray and black colors, those colors need to be more obvious to find shadows regions. Based on that, using temporal compression can find the shadow segmentation on images clearly.

3.4.2 Thresholding operation

Thersholding is a widely used technique for image segmentation. It is useful in discriminating forgrround from the background. Thresholding operation is used to convert multilevel gray scale image into a binary image. The advantage of obtaining first binary image is that it reduces the complexity of the data and simplifies the process of recognition and classification.

Here, the threshold determines shadow regions based on confidence map:

$$g(x,y) = \begin{cases} 0 & \text{if} \quad f(x,y) < T \\ 1 & \text{if} \quad f(x,y) \geq T \end{cases}$$

Where T represents threshold value, $f(x,y)$ represents confidence map image pixels, and $g(x,y)$ represents threshold image.

3.4.3 Comparison between automatic and manual detection

Accuracy is needed for automatic shadows detection algorithm. Consequently, the dice coefficient between automatic detection and manual segmentation is computing to demonstrate the accuracy of the results. It is often used to quantify the performance of image segmentation methods. Chapter 4 will describe the formula used and thus final results.

3.4.4 Random walks

Random walk is a widely used algorithm for image segmentation in the computer vision and medical image segmentation community [44] [42] [39] [45] [38]. In this thesis, a technique for detecting shadows in ultrasound images by calculating a per pixel confidence map which is employed within a random walks framework is proposed. The random walks algorithm was originally introduced for K-label image segmentation. The image is defined as an undirected weighted graph $G = (V, E)$ with an edge e spanning two vertices v_i and v_j denoted by e_{ij} . The weight of an edge e_{ij} is denoted by $w = (e_{ij})$ or w_{ij} that represents the likelihood of a random walk crossing that edge and the degree of a vertex i is $d_i = \sum w(e_{ij})$. The probability of a random walk starting at a pixel to reach the first K seed point is computed from the graph

Laplacian matrix, which is defined as:

$$L_{ij} = \begin{cases} d_i & \text{if } i = j \\ -w_{ij} & \text{if } v_i \text{and } v_j \text{ are adjacent nodes} \\ 0 & \text{otherwise} \end{cases} \tag{3.4}$$

where L_{ij} is indexed by vertices v_i and v_j. Different choices can be made for the weighting function w_{ij}, including the commonly applied Gaussian weighting $w_{ij} = \exp\left(-\beta \left(g_i - g_j\right)^2\right)$, where g_i is the pixel intensity at node i and β is a free parameter. Alternatively, the Laplacian matrix can also be constructed from the graph incidence matrix A and the diagonal matrix of edge weights C by $L = A^T C A$. Note that L is a sparse, symmetric, and semi-definite matrix.

An important matrix for describing graph problems is the Graph Laplacian, defined as:

$$L = A^T C A = D - W \tag{3.5}$$

D and W are defined as:

$$D = \begin{bmatrix} 2 & 0 & 0 & 0 \\ 0 & 2 & 0 & 0 \\ 0 & 0 & 2 & 0 \\ 0 & 0 & 0 & 2 \end{bmatrix} W = \begin{bmatrix} 0 & 1 & 1 & 0 \\ 1 & 0 & 0 & 1 \\ 1 & 0 & 0 & 1 \\ 0 & 1 & 1 & 0 \end{bmatrix} \tag{3.6}$$

The D matrix is referred to as the degree matrix and has the number of edges meeting at the node; i.e, the matrix is n by n and rows and columns represent the graph nodes. The matrix W is referred to as the adjacency matrix. The non-zero matrix entries describe which nodes in the n by n matrix share an edge. The diagonal is zero, as nodes are not adjacent to themselves. The resulting Weighted Graph Laplacian is

defined as:

$$L = A^T C A = \begin{bmatrix} -1 & -1 & 0 & 0 \\ 0 & 1 & 0 & -1 \\ 1 & 0 & -1 & 0 \\ 0 & 0 & 1 & 1 \end{bmatrix} \begin{bmatrix} c_1 & 0 & 0 & 0 \\ 0 & c_2 & 0 & 0 \\ 0 & 0 & c_3 & 0 \\ 0 & 0 & 0 & c_4 \end{bmatrix} \begin{bmatrix} -1 & 0 & 1 & 0 \\ -1 & 1 & 0 & 0 \\ 0 & 0 & -1 & 1 \\ 0 & -1 & 0 & 1 \end{bmatrix} \tag{3.7}$$

where c_1, c_2, c_3 and c_4 are the weights for the corresponding edges. Both the incidence and Laplacian matrix are highly interesting and have various properties. Subsequently, L is re-ordered and decomposed into blocks of marked M and unmarked nodes U:

$$L = \begin{bmatrix} L_M & B \\ B^T & L_U \end{bmatrix} \tag{3.8}$$

The explanation for the desired probabilities is obtained by solving the system of linear equations:

$$L_U x_U = -B^T x_M \tag{3.9}$$

where x_u represents the unknown probabilities for the unmarked nodes and x_m the known unit probabilities at the seed nodes. For multiple labels the previous equation becomes:

$$L_U X = -B^T M \tag{3.10}$$

The matrix sizes provide further intuition as:

$$L_{n\times n} = \begin{bmatrix} L_{M(K\times K)} & B_{K\times q} \\ B^T_{q\times K} & L_{U(q\times q)} \end{bmatrix}, L_{U(q\times q)} X_{q\times l} = -\beta^T_{q\times K} M_{K\times l} \tag{3.11}$$

where n is the number of nodes, k is the number of marked nodes, q is the number of unmarked nodes, and l is the number of labels. The system is solved for $l-1$ labels

as $\sum_i x_i^l = 1$.

3.5 Ultrasound confidence map

The confidence map is a probability density function on the new image, assigning each pixel of the new image a probability, which is the probability of the pixel color occurring in the object in the previous image [47]. Here, the random walk provides the desired solution to find the probability of the first pixel of reaching each of the virtual transducer elements, starting with the required seed placement procedure. Two constraints are integrated into the random walks framework with a new weighting function given by:

$$W_{ij} = \begin{cases} W_{ij}^H & \text{if } i,j \textit{ adjacent and } e_{ij} \epsilon E_H \\ W_{ij}^V & \text{if } i,j \textit{ adjacent and } e_{ij} \epsilon E_V \\ W_{ij}^D & \text{if } i,j \textit{ adjacent and } e_{ij} \epsilon E_D \\ 0 & \text{otherwise} \end{cases} \tag{3.12}$$

$$W_{ij}^H = \exp\left(-\beta\left(|c_i - c_j| + \gamma\right)\right) \tag{3.13}$$

$$W_{ij}^V = \exp\left(-\beta\left(|c_i - c_j|\right)\right) \tag{3.14}$$

$$W_{ij}^D = \exp\left(-\beta\left(|c_i - c_j| + \sqrt{2}.\gamma\right)\right) \tag{3.15}$$

$$c_i = g_i \exp\left(-\alpha l_i\right) \tag{3.16}$$

Where E_H, E_V, and E_D are the edge along the horizontal, vertical and diagonal graph direction respectively. Figure 3.3 is an illustration of the seed placement. The first row resembles the virtual transducer elements with the probabilities set to unity

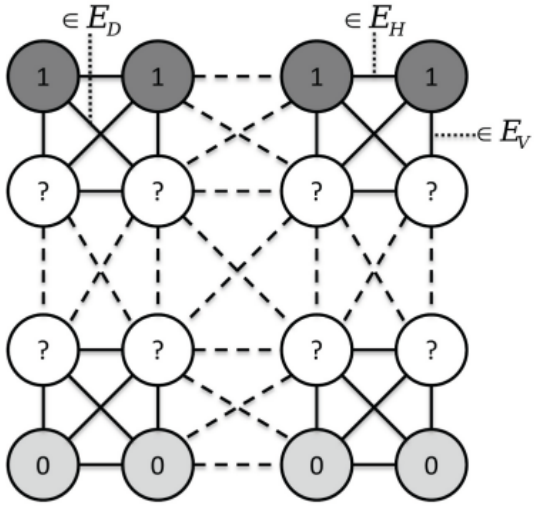

Figure 3.3: Random walks framework
[47]

(shaded dark gray). The last row resembles the 'no signal' region , i.e., the necessary boundary condition, with the probabilities set to zero (shaded bright gray). For all the nodes between the probability that a random walk starting from each node would first reach one of the virtual transducer elements is computed.

3.5.1 Confidence in shadow regions

Scanline integration is chosen, as it is a simple and commonly applied approach in ultrasound image processing for detecting shadow areas in the images [48]. The scanline integrated image S is given by

$$S\left(p,s\right) = S_M - \int_0^p G_Q * I(p,s)dx \tag{3.17}$$

where $I\left(p,s\right)$ is the image intensity at position p along the s scanline and G_Q is a Gaussian kernel of size 5; $\sigma = 2.0$, and $S_M = max\left(S\right)$, to evaluate the shadow detection capabilities of the confidence maps with a simple approach that only utilizes the maps and no further information. More specifically, shadow regions are defined by merely thresholding the confidence map for each image with:

$$S_i = \begin{cases} 1 & if C_i \leq T \\ 0 & otherwise \end{cases} \tag{3.18}$$

where $C_i \in [0..1]$ is the confidence value at pixel/node v_i and $T = 0.1$ is a heuristic threshold for determining the shadow region S. This simple approach has been chosen in order to evaluate the direct applicability of the confidence maps for shadow detection.

Algorithm 1 Random Walk

1: **Input:** An image represented $G = (V, E)$, as an undirected weighted graph, with edge e, spanning two vertices v_i and v_j.

2: Calculate the degree of a vertex i;
$d_i = \sum w\left(e_{ij}\right)$.

3: Calculate the graph Laplacian matrix;
$$L_{ij=}\begin{cases} d_i \\ -w_{ij}\,. \\ 0 \end{cases}$$

4: Use Gaussian weighting function;
$w_{ij} = exp\left(-\beta\left(g_i - g_j\right)^2\right)$.

5: Solve the system of linear equations;
$L_{UXU} = -B_{XM}$

6: **Output:** Random walks framework

Algorithm 2 The Prposed Method

1: **Input:** B-mode image ultrasound.
2: Compute attenuation weighting [47];
    A: image
    alpha: Attenuation coefficient.
3: Compute probabilities of confidence estimation with;
    seeds,labels: Seeds,labels for the random walks framework
    β : Random walks parameter
    γ : Horizontal penalty factor.
4: Index matrix with boundary padding.
5: Compute Laplacian matrix.
6: Select marked columns from Laplacian.
7: Select marked nodes.
8: Index of unmarked nodes.
9: Remove marked nodes from Laplacian by deleting rows and cols.
10: Adjust labels.
11: Find number of labels (K).
12: Define M matirx.
13: Compute confidence map with;
    data: Ultrasound data (one scanline per column)
    mode: 'B' mode data.
14: Default parameter settings.
15: Apply weighting directly to image.
16: Find confidence values.
17: Choose scanline integrated.
18: Apply temporal compression.
19: Use threshold operation.
20: Compare between automatic detection and manual segmentation approaches.
21: **Output:** Automatic shadows detection in ultrasound imaging.

Chapter 4

Experimental Results and Discussion

In this thesis, improving technology in ultrasound devices has made an essential contribution to the development of an emergency ultrasound program. The stationary and operationally complex devices historically associated with ultrasound have been replaced by a variety of highly portable and more intuitive machines. Hardware improvements have been accompanied by software enhancements, resulting in increased speed, flexibility, image quality and ease of use. These technological advancements have increased the practical utility of ultrasound and have allowed the movement of this technology from the laboratory to the bedside. As shown in figure 4.1, the system used here facilities the use of multiple Kinects for the purposes of motion and performance capturing. It can capture data from different viewpoints. Although a joint may be hidden from one Kinect, multiple Kinects provide a clear view by merging the RGB data and depth data received from different Kinects.

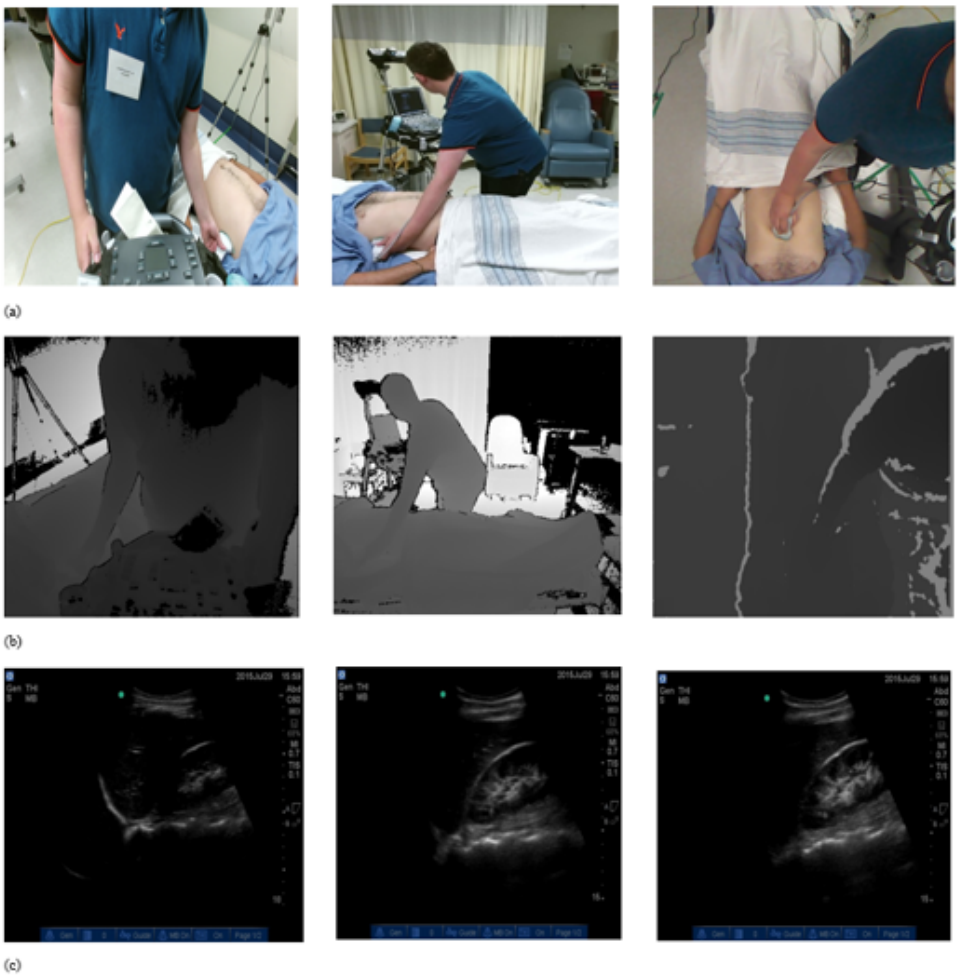

Figure 4.1: (a) RGB, (b) Depth data, (c) US images

The system designed shows evaluation of the motion tracking of the ultrasound transducer. Based on the synchronized ultrasound images with three Kinects, the performances of a novice, an intermediate and an expert sonographer inside an operating room can be differentiated. This is done by examining the ultrasound images in terms of noise and shadow detection.

4.1 Video Analysis

The following section outlines how studiocode is used to analyze video data of a sonographer inside an operating room. Many applications have used Studiocode Development Environment in medical research. In this project, Studiocode software is used because it is a really straightforward, easy to use data capture software, with a flexible style so it can be designed and used in any alignment with the performance and type of outcomes. In this work, multiple videos captured simultaneously are analyzed to see the probe movement in different angles, because although simulation is useful, it must show improvements in critical thinking and performance. Outcomes are needed and the studiocode software allows objective analysis of data so that the video file can be erased. This occurs after the data points of what occurred in specific measured behaviors are dropped. These can be displayed in an Excel spreadsheet which allows the important data to be kept while protecting the identity of the sonographers. The identifying video data can thus be securely stored as the pertinent information has already been extracted from the video.

4.1.1 Medical Checklist

FAST exam

The focused assessment with sonography for trauma FAST is one of the earliest applications of bedside sonography. This has been widely investigated and continues to be extremely useful, especially in the blunt abdominal and in certain instances it can be helpful in penetrating trauma as well as finding the key concepts in the fast exam [46]. More specifically, the FAST exam is positive or negative based on the presence of free fluid in abnormal locations, so the sonographer focuses on the potential spaces in the body where free fluid tends to accumulate.

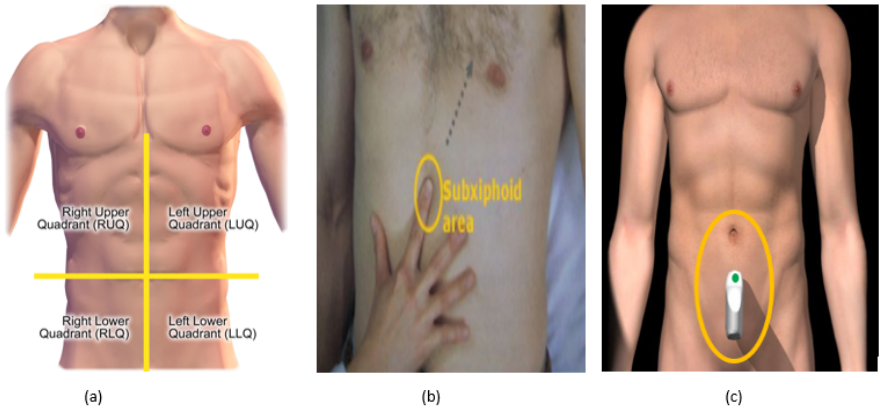

Figure 4.2: (a)RUQ, LUQ, RLQ, LLQ (b)Subxiphoid area, (c) Subrapubic area

As a part of the FAST exam, the doctors evaluate potential spaces as follows (See Fig 4.2):

- The right upper quadrant (RUQ),
- The left upper quadrant (LUQ),
- The subxiphoid area and
- The suprapubic area.

The video data was reviewed using Studiocode to identify specific tasks in the checklist with the objective of grading trainee performance. Figure 4.3 shows an example of four images extracted from synchronized video designed to highlight transducer movement throughout performance of the FAST exam. The coding input window enables the items on the checklist to be observed when the doctor performs the FAST exam (See Fig 4.4) with the code buttons used to mark points in the timeline based on the location in the video. One of the most important components of this video analysis software is the timeline (See Fig 4.5). The timeline highlights the tagging of specific checklist items enabling assessment of sonographer performance.

Figure 4.3: Stacked timeline

.

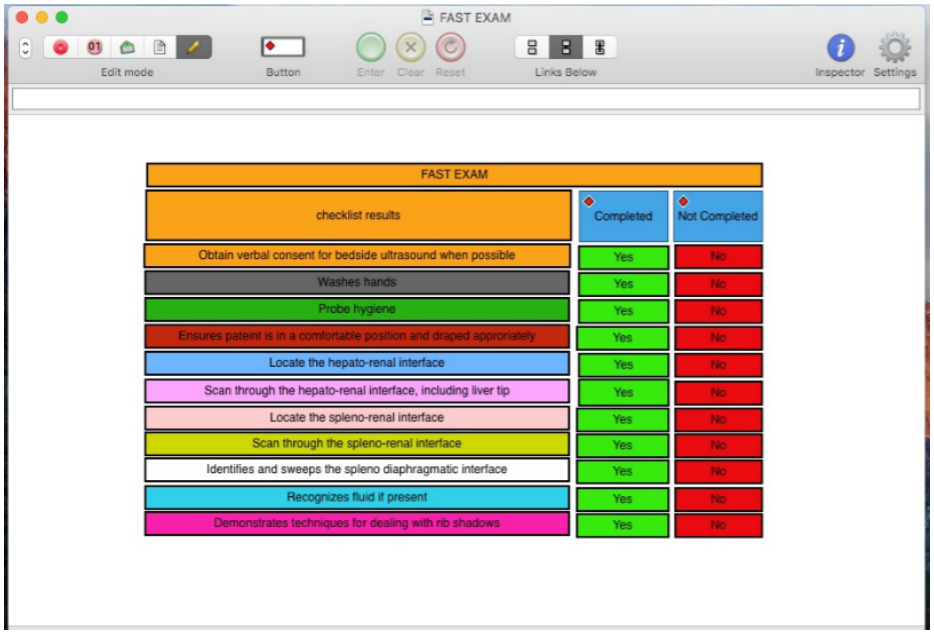

Figure 4.4: Coding input window

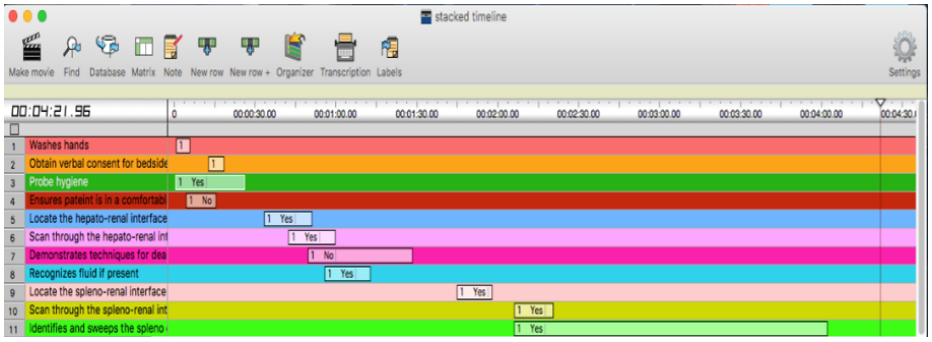

Figure 4.5: Timeline

As mentioned previously, it is demonstrated how these video data have been studied. Figure 4.5 observes the timeline instances. Each instance has a video of the doctors' scanning action, and based on that it can be decided if the checklist is completed or not. Consequently, use a Studiocode software helps to differentiate between a novice, an intermediate and an expert sonographer based on their scanning.

In order to collect synchronized data, a system to sync three multiple cameras was developed. In addition to the Studiocode analysis described above, the ultrasound image data was studied in two aspects:

(1) Speckle noise reduction.

(2) Automatic detection of shadows.

The approach used to investigate these topics is discussed in the following sections.

4.2 Image Filtering

The purpose of applying multiple filters on the image is to compare and investigate the algorithms to illustrate which one is appropriate. Using an ultrasound image of the neck vessels (See Fig 4.6), noise images have been generated.

4.2.1 Median filter

A 3×3 window size is used for this algorithm. As shown in figure 4.7, a median filter excludes noise for a better quality image. To be exact, the noise disappears without losing important details when a median filter in a Poisson noise image is applied. However, the damaging effects are more visible with Gaussian and Salt & Pepper and Speckle noise.

4.2.2 Gaussian filter

The Gaussian filter behaves quite similarly to a median filter with the same window size. However, the MSE was low between the noisy image and the filtered image suggesting that no significant improvement was made, as shown in figure 4.8.

4.2.3 Average filter

The Average filter was observed to remove Speckle and Poisson noise from images successfully. Its performance was unsatisfactory on both the Salt & Pepper and speckle noise images (See Fig 4.9). According to the MSE, the Average filter has good results to eliminate the noise on both the speckle and Poisson noise images [51].

4.2.4 Log filter

A log filter was shown to be unsuitable in these different types of noise images, with the images clearly being demonstrated to be worse visually and the resultant MSE as shown in Figure 4.10.

4.2.5 Wiener filter

No meaningful improvement was noted with the application of the Wiener filter. Figure 4.11 shows the resultant images. The MSE for the Wiener filter was the highest when compared to other filters explored in this research.

4.2.6 N-D filter

The results of the N-D filter are clearly seen in Figure 4.12. This filter does eliminate noise. However, results in a blurring of the image features.

Image quality metrics

Tables 4.1, 4.2, 4.3 and 4.4 indicate the performance of the filters under various noise conditions. In the image quality metrics, the lowest mean-squared error (MSE) means the performance of an image is the best, signifying a high quality of image. In contrast, the highest peak signal-to-noise ratio (PSNR), and signal to noise ratio (SNR) indicate the best performance of an image which leads to the best image quality. In this study, it is confirmed that Median and Average filters can be used and improved for ultrasound images. Developing the combination of these two filters to enhance the images can be taken into consideration for future research. However, the Log and Wiener filter did not produce acceptable results during our study.

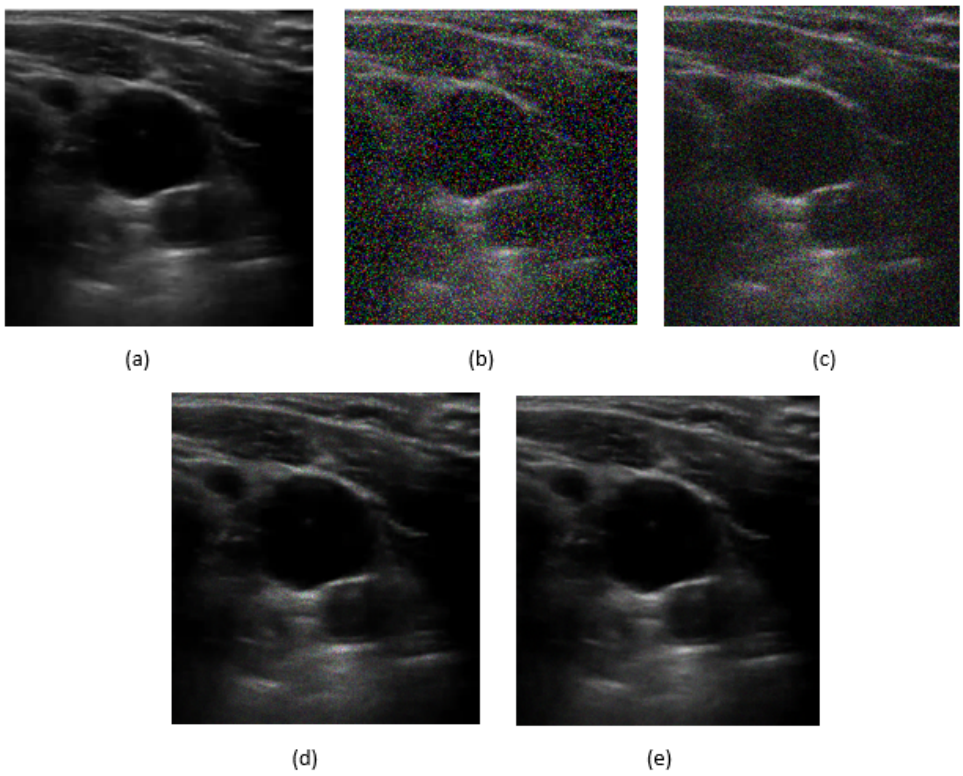

Figure 4.6: (a) Reference image, (b) Salt & Pepper noise, (c) Gaussian noise, (d) Speckle noise, (e) Poisson noise

.

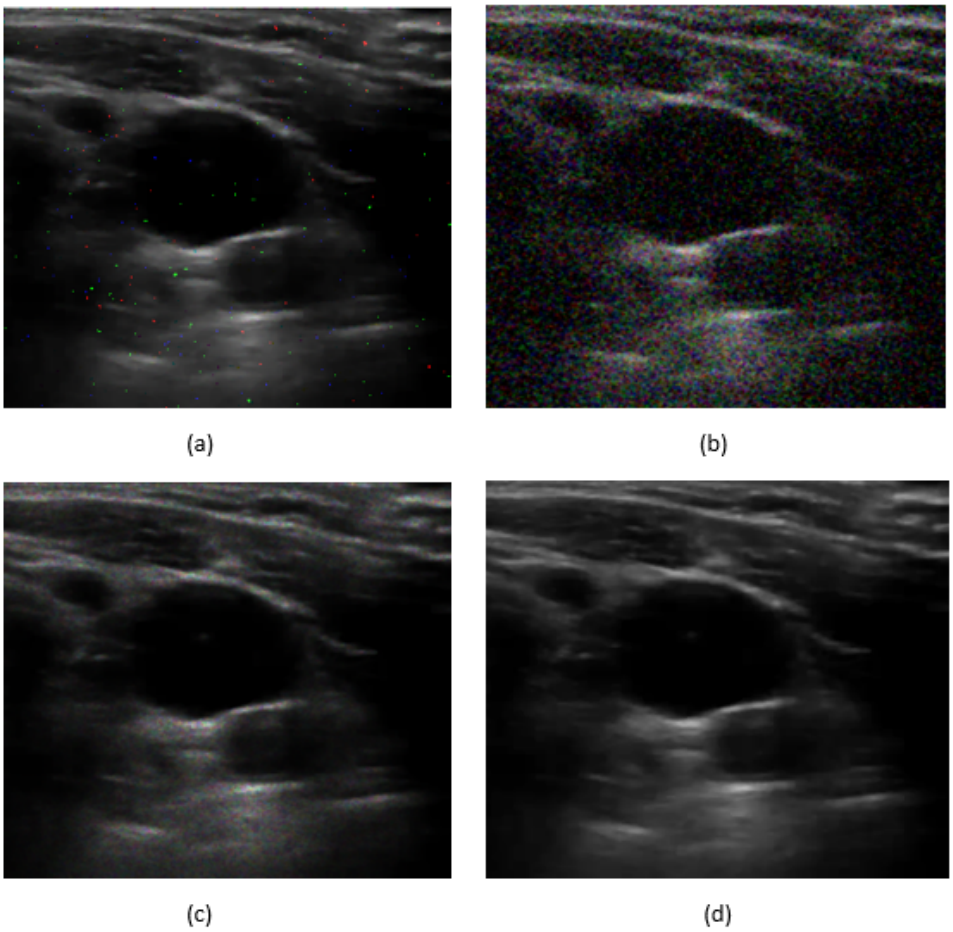

Figure 4.7: Images after applying Median filter with different noises (a) Salt & Pepper noise, (b) Gaussian noise , (c) Speckle noise(d) Poisson noise

.

Table 4.1: Metrics values of image quality parameters by filters with Salt & Pepper noise applied on the cell image.

Filter types	MSE	SNR	PSNR
Median	8.5371	225.5441	250.8055
Gaussian	0.0820	166.0247	191.2861
Average	0.0096	193.9681	219.2295
Log	182.6346	65.5973	90.8587
Wiener	256.4563	61.1743	86.4357
N-D	0.0104	192.9801	218.2415

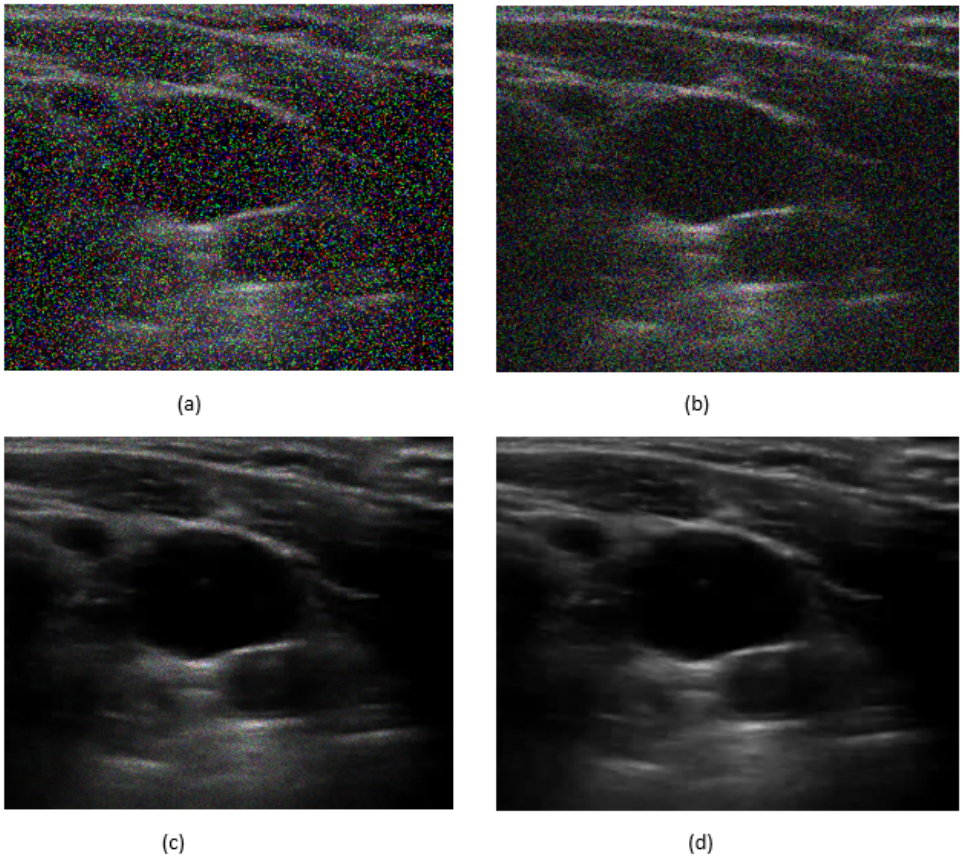

Figure 4.8: Images after applying Gaussian filter with different noises (a) Salt & Pepper noise, (b) Gaussian noise , (c) Speckle noise(d) Poisson noise

Table 4.2: Metrics values of image quality parameters by filters with Gaussian noise applied on the cell image.

Filter types	MSE	SNR	PSNR
Median	0.0062	199.6332	224.8946
Gaussian	0.0308	178.7955	204.0569
Average	0.0048	203.0969	228.3583
Log	65.9092	78.8763	104.1377
Wiener	192.7809	64.8933	90.1547
N-D	0.0073	197.4776	222.7390

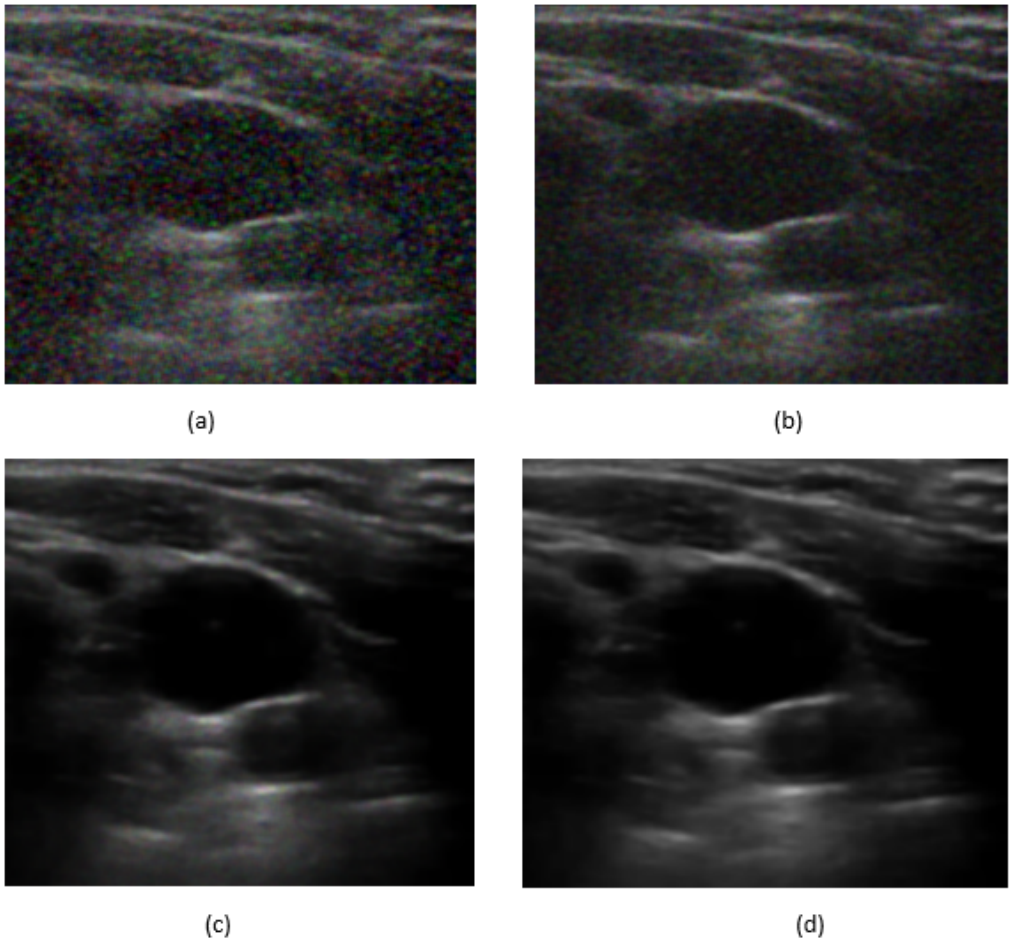

Figure 4.9: Images after applying Average filter with different noises (a) Salt & Pepper noise, (b) Gaussian noise , (c) Speckle noise(d) Poisson noise

Table 4.3: Metrics values of image quality parameters by filters with Multiplicative noise applied on the cell image.

Filter types	MSE	SNR	PSNR
Median	3.8182	235.9911	261.2525
Gaussian	0.0013	220.0353	245.2967
Average	2.6053	240.9694	266.2308
Log	3.7188	116.3326	141.5940
Wiener	119.6964	71.1022	96.3636
N-D	0.0039	205.5763	230.8377

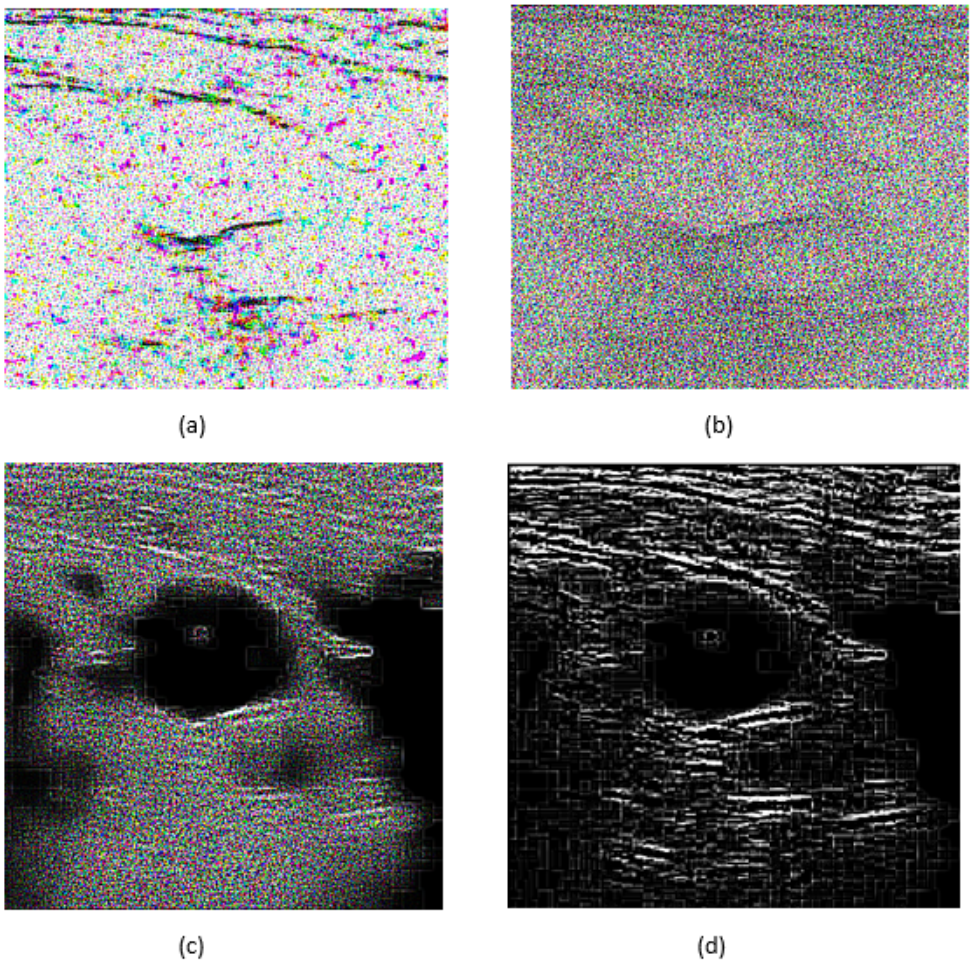

Figure 4.10: Images after applying Log filter with different noises (a) Salt & Pepper noise, (b) Gaussian noise , (c) Speckle noise(d) Poisson noise

Table 4.4: Metrics values of image quality parameters by filters with Poisson noise applied on the cell image.

Filter types	MSE	SNR	PSNR
Median	2.3757e-05	272.1706	297.4320
Gaussian	1.2615e-13	520.4180	545.6794
Average	2.0890e-04	243.8463	269.1077
Log	0.6090	139.9060	165.1674
Wiener	119.4731	71.1265	96.3879
N-D	0.0039	205.6322	230.8936

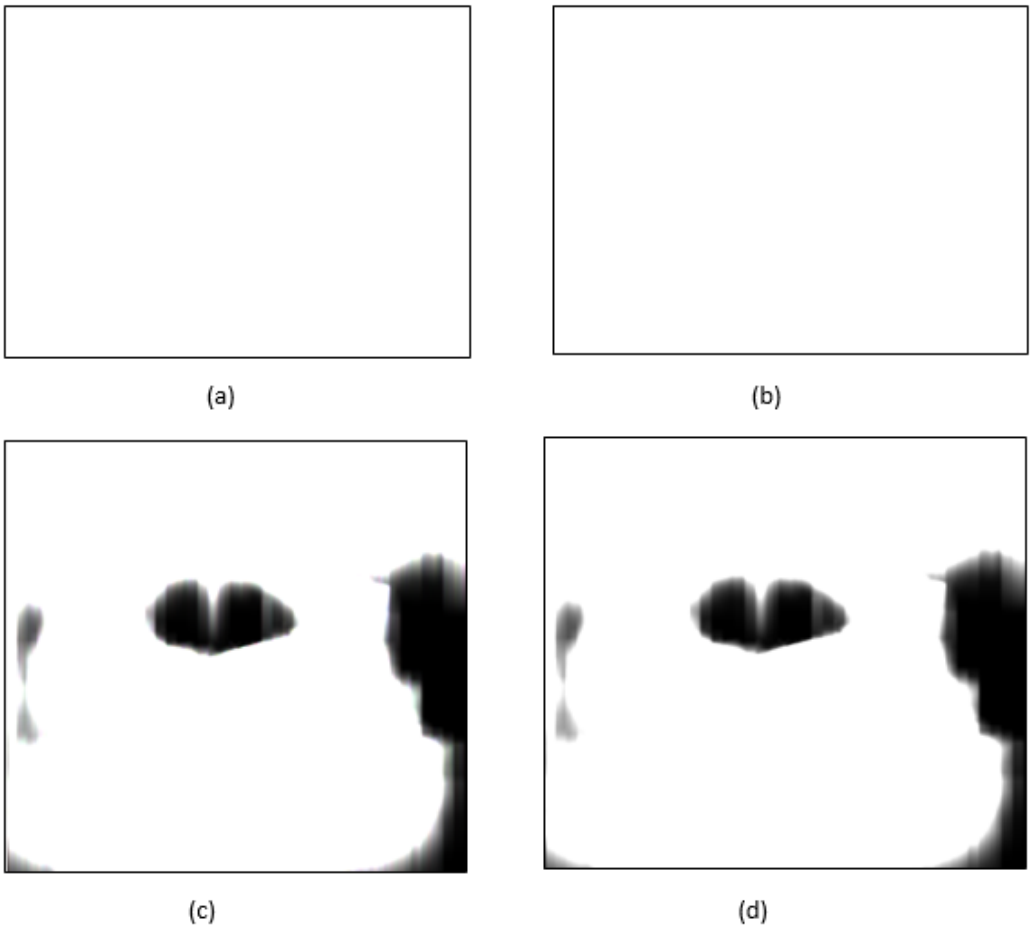

Figure 4.11: Images after applying Wiener filter with different noises (a) Salt & Pepper noise, (b) Gaussian noise , (c) Speckle noise(d) Poisson noise

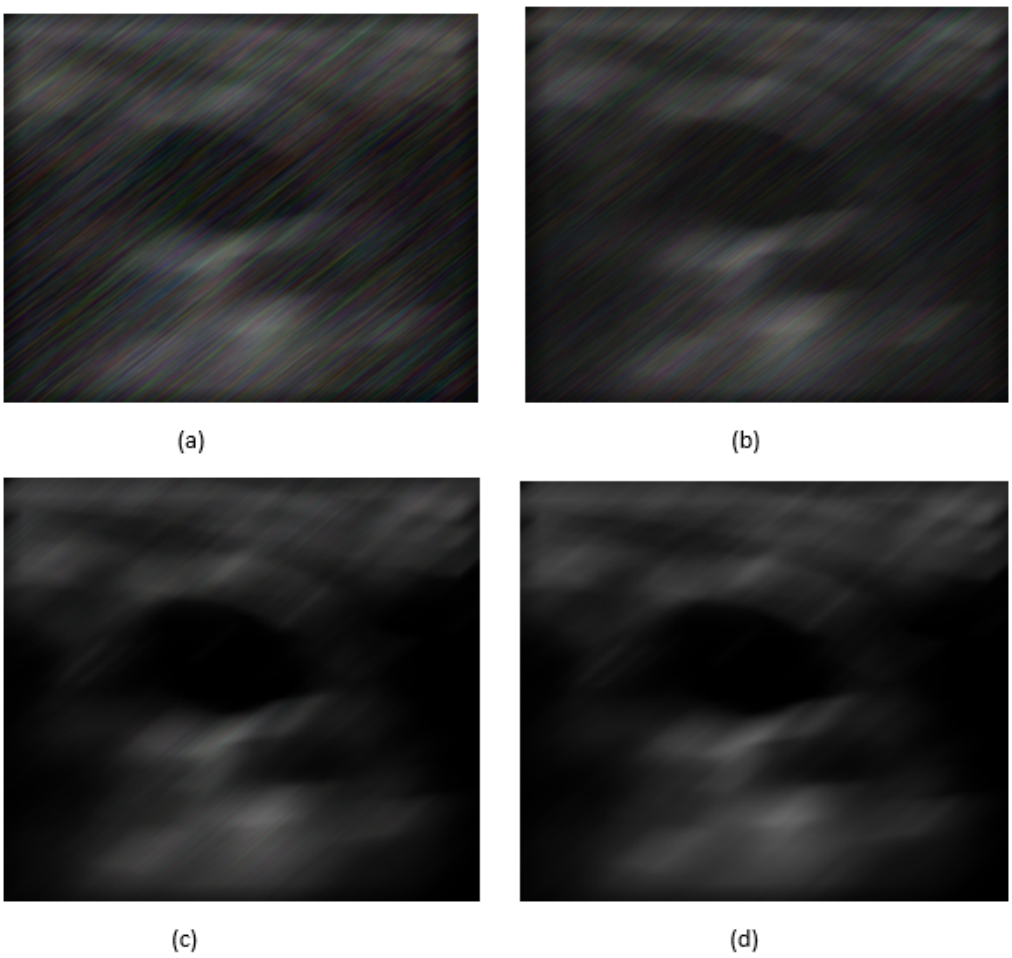

Figure 4.12: Images after applying N-D filter with different noises (a) Salt & Pepper noise, (b) Gaussian noise , (c) Speckle noise(d) Poisson noise

.

4.3 Shadow detection regions

This section presents the results of the research into confidence maps used for automatic shadow detection in ultrasound images (See Fig 4.13). Three parameters, alpha α, beta β and gamma γ are defined as follows.

- α affects the likelihood of vertical random walks. It effectively scales the confidence along the vertical graph direction in random walks formulation. Figure 4.14 shows an example of the effect of alpha on estimating a confidence map. In this experiment, a constant value of $\alpha = 2$ is set, achieving good qualitative and quantitative results.

- β affects on the robustness and accuracy of the segmentation; a constant value of $\beta = 90$ is set for this experiment. Figure 4.15 shows an example of the effect that beta has on estimating a confidence map.

- γ penalizes horizontal and diagonal random walks. The effective of gamma values in figures 4.16 is determined, it can be confirmed that Gamma's value can affect the estimation of images in a confidence map.

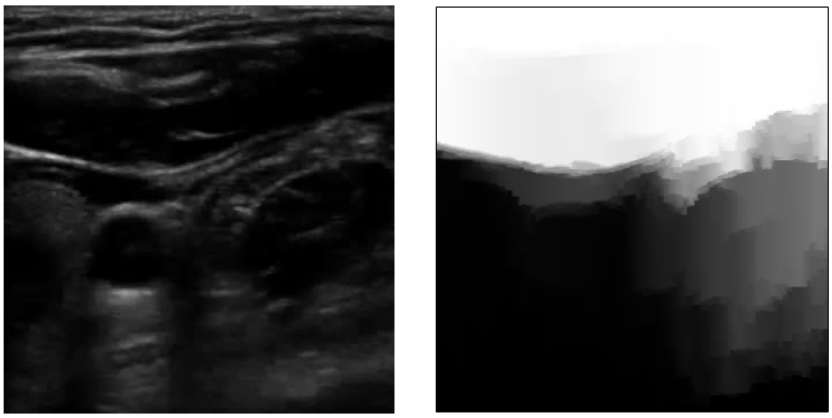

Figure 4.13: (a) B-mode image, (b) The corresponding confidence map

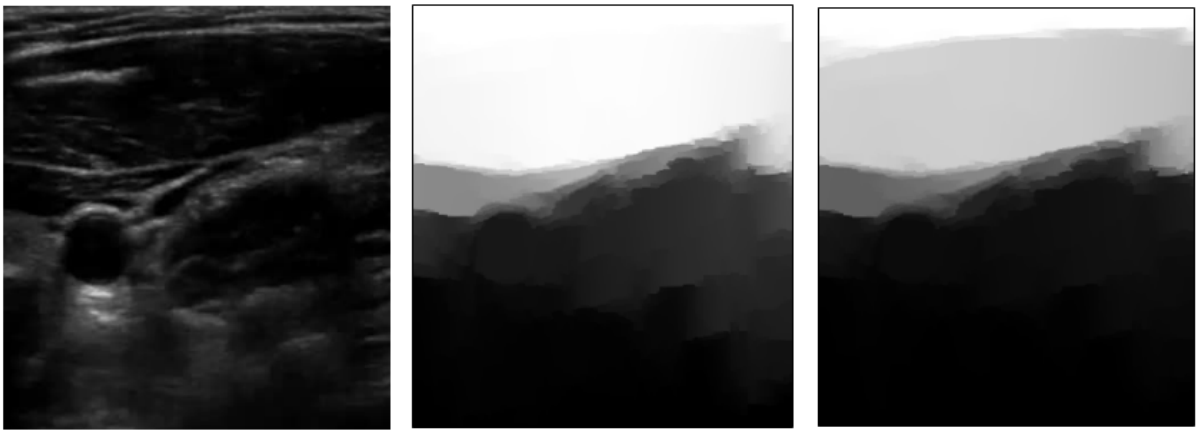

Figure 4.14: Different values of α can affect the confidence map (a) US image, (b) $\alpha = 2$,(c) $\alpha = 6$

Figure 4.15: (a) US image, (b) $\beta = 90$, (c) $\beta = 120$

Figure 4.16: (a) US image, Different values of gammas effective: (b) $\gamma = 0.05$, (c) $\gamma = 0.09$

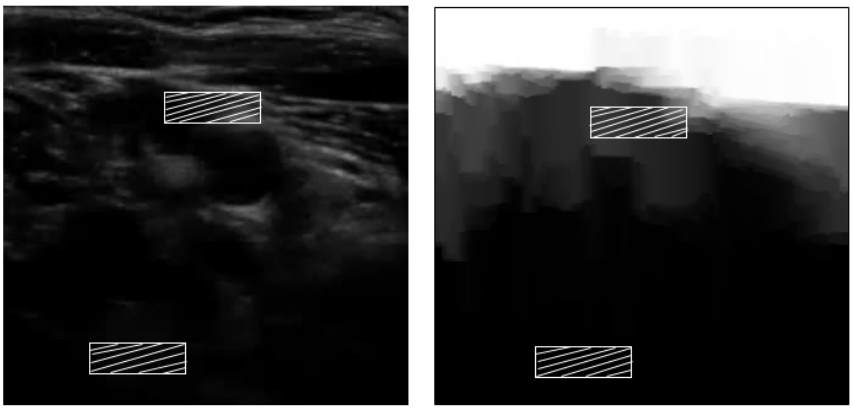

Figure 4.17: Boxes in the images indicate regions of high and low confidence

In this thesis, a confidence estimation method is proposed to emphasize the uncertainty of shadowed regions. Consequently, the method is evaluated by assessing its reliability in estimating low confidence for regions that are known to be of low confidence, which has been indicated by shadow regions, as shown in figure 4.17.

More specifically, the very dark depiction of low confidence in this method indicates shadows are detected. Figure 4.18 shows the results of the confidence map and the threshold determines the shadow regions. The algorithm works fully automatically as can be indicated by the low confidence map and high confidence map (shadow regions and unreliable image information) as shown in figure 4.19.

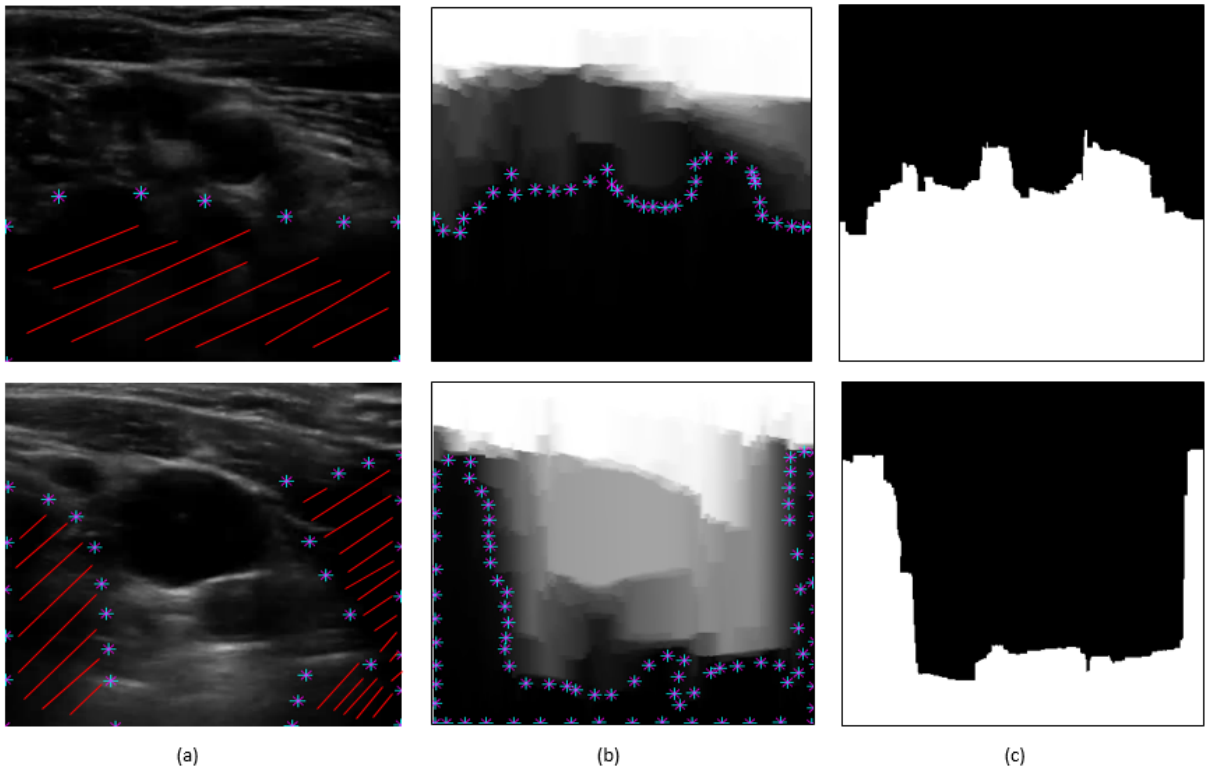

Figure 4.18: (a) US images with shadowed area below dot stars include red lines , (b)The corresponding confidence maps for detecting shadows automatically, (c) The threshold determines shadow regions based on the confidence map

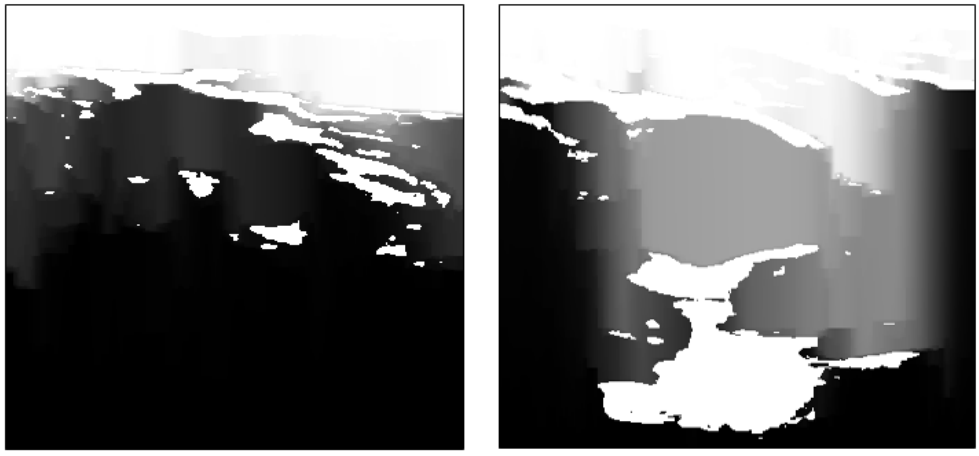

Figure 4.19: Confidence maps for US images indicated between shadow regions (LC) which are the very dark black regions and unreliable image information (HC)

.

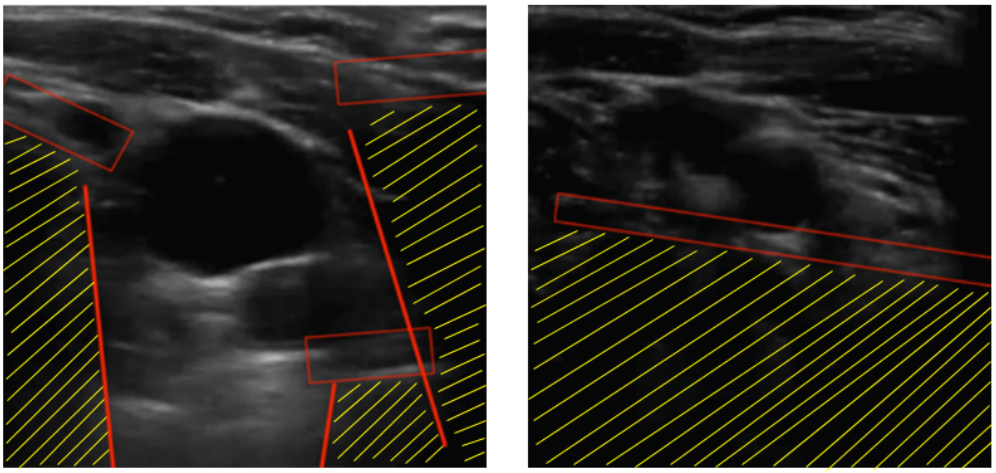

Figure 4.20: Expert manual shadow segmentation

.

For a quantitative evaluation, an expert was asked to manually segment the shadow regions in ultrasound images as shown in figure 4.20. The Dice coefficient between manual and confidence segmentations was computed. The Dice coefficient is defined by:

$$DICE = \frac{2TP}{2TP + FP + FN} \tag{4.1}$$

where the three cardinalities are defined as follows:

- True positive (TP) presents pixels of shadow areas for both manual and automatic detection.
- False positive (FP) presents pixels of shadow areas with manual detection.
- False negative (FN) presents pixels for incorrect shadow areas that are not indicated by manual and automatic detection.

Table 4.5: Dice coefficient results of shadows between manual and automatic segmentation

Data	$\gamma = 0.2$	$\gamma = 0.3$	$\gamma = 0.4$	$\gamma = 0.5$	$\gamma = 0.6$	$\gamma = 0.7$	$\gamma = 0.8$	$\gamma = 0.9$
PTP	1	1	1	0.9996	0.9978	0.9953	0.9945	0.9934
PFP	0.1247	0.1405	0.1446	0.1481	0.1512	0.1476	0.1417	0.1359
PFN	0	0.11	0.12	0.14	0.19	0.10	0.11	0.17

Table 4.6: Dice coefficient results of shadows between manual and automatic segmentation

Data	$\gamma = 0.2$	$\gamma = 0.3$	$\gamma = 0.4$	$\gamma = 0.5$	$\gamma = 0.6$	$\gamma = 0.7$	$\gamma = 0.8$	$\gamma = 0.9$
PTP	0.8461	0.8454	0.8439	0.8596	0.8641	0.9061	0.9265	0.9628
PFP	0.1692	0.1730	0.1771	0.1742	0.1738	0.1750	0.1711	0.1692
PFN	0.22	0.22	0.21	0.22	0.16	0.15	014	0.18

Based on the results in tables 4.5 and 4.6, in general, the random walks algorithm obtained good results for automatic shadow detection. To be exact, it is suggested that for $\gamma = 0.9$ the confidence map quite effective at shadow detection for the images evaluated. Consequently, the values of probability of true positive and probability of false positive provide a good quality score which indicates a confidence map system works very well with shadowing in ultrasound images. By comparing the expert and automatic method, it is suggested that the confidence map can be useful for automatic shadow detection.

Chapter 5

Conclusions and Future Work

The aim of the current study was to develop a methodology to collect data inside an operating room to assess sonographers skill have the appropriate to perform point of care ultrasound. An automated system to sync multiple depth cameras with ultrasound imaging is proposed in this thesis.

In the proposed methodology, the receiving data from depth cameras have been analyzed by using studiocode to differentiate between novice, immediate and expert sonographers using a checklist.

Next, my efforts focused on the assessment of speckle noise reduction and shadow detection as a further means to assess ultrasound image quality.

Some techniques that can deal with suppression of speckle noise in US imaging have been presented. In addition, several methods for smoothing were compared to determine which one was more appropriate. Subsequently, the image used quality metrics to test the methods' performance and demonstrate the benefits of each one.

Furthermore, an automated method to detect shadows in US images by a confidence map using random walks has been studied. By computing the Dice coefficient, automatic and manual shadow segmentation based on results have been compared.

5.1 Future Work

The current study can be further extended to work with and track ultrasound videos for further analysis in different studies. Tracking the object and detecting important details in US images will assist for patient diagnostics. Selecting a constant value of Gamma parameter requires a balance between having distinct confidence and having minimal discontinuities in the horizontal direction.

Simulation studies performed in this study show a good prospect of proposed ultrasound imaging analysis. Consequently, the method requires more experimental validation to increase and improve the output of the ultrasound imaging quality.

Bibliography

[1] Case, T. D. (1998). Ultrasound physics and instrumentation. Surgical Clinics of North America, 78(2), 197-217.

[2] Rabbani, H., Vafadust, M., Abolmaesumi, P., & Gazor, S. (2008). Speckle noise reduction of medical ultrasound images in complex wavelet domain using mixture priors. IEEE transactions on biomedical engineering, 55(9), 2152-2160.

[3] Michailovich, O. V., & Tannenbaum, A. (2006). Despeckling of medical ultrasound images. ieee transactions on ultrasonics, ferroelectrics, and frequency control, 53(1), 64-78.

[4] Miles, R. (2012). Start Here! Learn the Kinect API. Pearson Education.

[5] Roomi, S. M. M., & Rajee, R. J. (2011, June). Speckle noise removal in ultrasound images using Particle Swarm Optimization technique. In Recent Trends in Information Technology (ICRTIT), 2011 International Conference on (pp. 926-931). IEEE.

[6] Huang, Q. H., & Zheng, Y. P. (2008). Volume reconstruction of freehand three-dimensional ultrasound using median filters. Ultrasonics, 48(3), 182-192.

[7] Wu, B., Zhang, Q., Ye, P., & Huang, Q. (2014, October). A Kinect-based scan path planning method for ultrasound imaging. In Biomedical Engineering and Informatics (BMEI), 2014 7th International Conference on (pp. 556-561). IEEE.

[8] Shotton, J., Sharp, T., Kipman, A., Fitzgibbon, A., Finocchio, M., Blake, A., ... & Moore, R. (2013). Real-time human pose recognition in parts from single depth images. Communications of the ACM, 56(1), 116-124.

[9] Cheng, L., Sun, Q., Su, H., Cong, Y., & Zhao, S. (2012, May). Design and implementation of human-robot interactive demonstration system based on Kinect. In Control and Decision Conference (CCDC), 2012 24th Chinese (pp. 971-975). IEEE.

[10] Ren, Z., Meng, J., Yuan, J., & Zhang, Z. (2011, November). Robust hand gesture recognition with kinect sensor. In Proceedings of the 19th ACM international conference on Multimedia (pp. 759-760). ACM.

[11] Kean, S., Hall, J., & Perry, P. (2011). Meet the Kinect: An introduction to programming natural user interfaces. Apress.

[12] Izadi, S., Kim, D., Hilliges, O., Molyneaux, D., Newcombe, R., Kohli, P., ... & Fitzgibbon, A. (2011, October). KinectFusion: real-time 3D reconstruction and interaction using a moving depth camera. In Proceedings of the 24th annual ACM symposium on User interface software and technology (pp. 559-568). ACM.

[13] Hellier, P., Coupé, P., Meyer, P., Morandi, X., & Collins, D. L. (2008, May). Acoustic shadows detection, application to accurate reconstruction of 3D intra-operative ultrasound. In Biomedical Imaging: From Nano to Macro, 2008. ISBI 2008. 5th IEEE International Symposium on (pp. 1569-1572). IEEE.

[14] Newcombe, R. A., Izadi, S., Hilliges, O., Molyneaux, D., Kim, D., Davison, A. J., ... & Fitzgibbon, A. (2011, October). KinectFusion: Real-time dense surface mapping and tracking. In Mixed and augmented reality (ISMAR), 2011 10th IEEE international symposium on (pp. 127-136). IEEE.

[15] Huang, Q., Huang, Y., Hu, W., & Li, X. (2015). Bezier interpolation for 3-D freehand ultrasound. IEEE Transactions on Human-Machine Systems, 45(3), 385-392.

[16] Qiu, T., Wen, T., Qin, W., Gu, J., & Wang, L. (2011, November). Freehand 3D ultrasound reconstruction for image-guided surgery. In Bioelectronics and Bioinformatics (ISBB), 2011 International Symposium on (pp. 147-150). IEEE.

[17] Basij, M., Moallem, P., Yazdchi, M., & Mohammadi, S. (2012, October). Automatic shadow detection in intra vascular ultrasound images using adaptive thresholding. In Systems, Man, and Cybernetics (SMC), 2012 IEEE International Conference on (pp. 2173-2177). IEEE.

[18] Hirakawa, K., & Parks, T. W. (2006). Image denoising using total least squares. IEEE Transactions on image processing, 15(9), 2730-2742.

[19] Nadernejad, E., Karami, M. R., Sharifzadeh, S., & Heidari, M. (2009). Despeckle filtering in medical ultrasound imaging. Contemporary Engineering Sciences, 2(1), 17-36.

[20] Treece, G., Prager, R., & Gee, A. (2005). Ultrasound attenuation measurement in the presence of scatterer variation for reduction of shadowing and enhancement. IEEE transactions on ultrasonics, ferroelectrics, and frequency control, 52(12), 2346-2360.

[21] Nadernejad, E., Karami, M. R., Sharifzadeh, S., & Heidari, M. (2009). Despeckle filtering in medical ultrasound imaging. Contemporary Engineering Sciences, 2(1), 17-36.

[22] Perona, P., & Malik, J. (1990). Scale-space and edge detection using anisotropic diffusion. IEEE Transactions on pattern analysis and machine intelligence, 12(7), 629-639.

[23] Yang, L., Zhang, L., Dong, H., Alelaiwi, A., & El Saddik, A. (2015). Evaluating and improving the depth accuracy of Kinect for Windows v2. IEEE Sensors Journal, 15(8), 4275-4285.

[24] Drukker, K., Giger, M. L., & Mendelson, E. B. (2003). Computerized analysis of shadowing on breast ultrasound for improved lesion detection. Medical Physics, 30(7), 1833-1842.

[25] Madabhushi, A., Yang, P., Rosen, M., & Weinstein, S. (2006, August). Distinguishing lesions from posterior acoustic shadowing in breast ultrasound via non-linear dimensionality reduction. In Engineering in Medicine and Biology Society, 2006. EMBS'06. 28th Annual International Conference of the IEEE (pp. 3070-3073). IEEE.

[26] Leroy, A., Mozer, P., Payan, Y., & Troccaz, J. (2004). Rigid registration of freehand 3D ultrasound and CT-scan kidney images. Medical Image Computing and Computer-Assisted Intervention–MICCAI 2004, 837-844.

[27] Penney, G. P., Blackall, J. M., Hamady, M. S., Sabharwal, T., Adam, A., & Hawkes, D. J. (2004). Registration of freehand 3D ultrasound and magnetic resonance liver images. Medical image analysis, 8(1), 81-91.

[28] Loizou, C. P., & Pattichis, C. S. (2008). Despeckle filtering algorithms and software for ultrasound imaging. Synthesis lectures on algorithms and software in engineering, 1(1), 1-166.

[29] Adam, D., Beilin-Nissan, S., Friedman, Z., & Behar, V. (2006). The combined effect of spatial compounding and nonlinear filtering on the speckle reduction in ultrasound images. Ultrasonics, 44(2), 166-181.

[30] Behar, V., Adam, D., & Friedman, Z. (2003). A new method of spatial compounding imaging. Ultrasonics, 41(5), 377-384.

[31] Stippel, G., Philips, W., & Lemahieu, I. (2002). A new denoising technique for ultrasound images using morphological properties of speckle combined with tissue classifying parameters. In Proc. SPIE (Vol. 4687, p. 325).

[32] Bernstein, R. (1987). Adaptive nonlinear filters for simultaneous removal of different kinds of noise in images. IEEE Transactions on Circuits and Systems, 34(11), 1275-1291.

[33] Santos Filho, E., Saijo, Y., Tanaka, A., & Yoshizawa, M. (2008). Detection and quantification of calcifications in intravascular ultrasound images by automatic thresholding. Ultrasound in medicine & biology, 34(1), 160-165.

[34] Karaman, M., Kutay, M. A., & Bozdagi, G. (1995). An adaptive speckle suppression filter for medical ultrasonic imaging. IEEE transactions on medical imaging, 14(2), 283-292.

[35] Abd-Elmoniem, K. Z., Youssef, A. B., & Kadah, Y. M. (2002). Real-time speckle reduction and coherence enhancement in ultrasound imaging via nonlinear anisotropic diffusion. IEEE Transactions on Biomedical Engineering, 49(9), 997-1014.

[36] Tolba, A. S. (2002). Wavelet packet compression of medical images. Digital Signal Processing, 12(4), 441-470.

[37] Chen, Y., Broschat, S. L., & Flynn, P. J. (1996). Phase insensitive homomorphic image processing for speckle reduction. Ultrasonic imaging, 18(2), 122-139.

[38] Grady, L. (2006). Random walks for image segmentation. IEEE transactions on pattern analysis and machine intelligence, 28(11), 1768-1783.

[39] Zhang, J., Zheng, J., & Cai, J. (2011). Interactive mesh cutting using constrained random walks. IEEE Transactions on Visualization and Computer Graphics, 17(3), 357-367.

[40] Duda, R. O., & Hart, P. E. (1972). Use of the Hough transformation to detect lines and curves in pictures. Communications of the ACM, 15(1), 11-15.

[41] Otsu, N. (1979). A threshold selection method from gray-level histograms. IEEE transactions on systems, man, and cybernetics, 9(1), 62-66.

[42] Sun, X., Rosin, P. L., Martin, R. R., & Langbein, F. C. (2008). Random walks for feature-preserving mesh denoising. Computer Aided Geometric Design, 25(7), 437-456.

[43] Akkasaligar, P. T., & Biradar, S. (2014, October). Classification of medical ultrasound images of kidney. In IJCA Proceedings on International Conference on Information and Communication Technologies (ICICT) (Vol. 3, pp. 24-28).

[44] Shen, R., Cheng, I., Li, X., & Basu, A. (2008, December). Stereo matching using random walks. In Pattern Recognition, 2008. ICPR 2008. 19th International Conference on (pp. 1-4). IEEE.

[45] Grady, L., Schiwietz, T., Aharon, S., & Westermann, R. (2005, September). Random walks for interactive alpha-matting. In Proceedings of VIIP (Vol. 2005, pp. 423-429).

[46] Reardon, R. (2013). Ultrasound in trauma–the FAST exam. Focused assessment with sonography in trauma. Ultrasound Guide to Emergency Physicians. http://www. sonoguide. com/FAST. html.

[47] Karamalis, A., Wein, W., Klein, T., & Navab, N. (2012). Ultrasound confidence maps using random walks. Medical image analysis, 16(6), 1101-1112.

[48] Cobbold, R. S. (2006). Foundations of biomedical ultrasound. Oxford University Press.

[49] Cosby, K. S., & Kendall, J. L. (Eds.). (2006). Practical guide to emergency ultrasound. Lippincott Williams & Wilkins.

[50] Mssedi, S., Salah, M. B., Abdelfattah, R., & Mitiche, A. (2011, September). Extraction of road network using amodified active contour approach. In Image Processing (ICIP), 2011 18th IEEE International Conference on (pp. 2929-2932). IEEE.

[51] Hamad, A. H., Muhammad, H. O., & Yaba, S. P. (2014). De-noising of medical images by using some filters. Int. Journal Of Biotechnology Research, 2014.

[52] Tavares, R. S., Chirinos, J. M. M., Abe, L. I., Gotoh, T., Kagei, S., Iwasawa, T., & Tsuzuki, M. D. S. G. (2011, August). Temporal segmentation of lung region from MRI sequences using multiple active contours. In Engineering in Medicine and Biology Society, EMBC, 2011 Annual International Conference of the IEEE (pp. 7985-7988). IEEE.

[53] Chan, T. F., & Vese, L. A. (2001). Active contours without edges. IEEE Transactions on image processing, 10(2), 266-277.

[54] Noll, M., Puhl, J., & Wesarg, S. (2014, July). Enhanced Shadow Detection for 3D Ultrasound. In Bildverarbeitung für die Medizin (pp. 234-239).

[55] Acharyya, A. (Ed.). (2016). Foundations and Frontiers in Computer, Communication and Electrical Engineering: Proceedings of the 3rd International Conference C2E2, Mankundu, West Bengal, India, 15th-16th January, 2016. CRC Press.